

Physical Processes Leading to Extreme ~~day-to-day~~Day-to-Day Temperatures Changes, Part I: Present-day Climate

Kalpana Hamal and Stephan Pfahl

5 Institut für Meteorologie, Freie Universität Berlin, 12165 Berlin., Germany

Correspondence to: Kalpana Hamal (k.hamal@fu-berlin.de)

Abstract

Extreme temperature changes from one day to another, either associated with warming or cooling, can have a significant impact on health, the environment, and society. Previous studies have quantified that such day-to-day temperature (DTDT)
10 ~~change~~variations are typically more pronounced in ~~the extratropics compared to the~~ extratropics than the tropics-tropical zones. However, the underlying physical processes and the relationship between extreme events and the large-scale atmospheric circulation remain poorly understood. Here, these processes are investigated for different locations around the globe based on ~~observation~~, ERA5 reanalysis data, and Lagrangian backward trajectory calculations. We show that extreme DTDT changes in the extratropics are generally associated with changes in air mass transport, ~~in particular~~particularly shifts
15 from warmer to colder air ~~parcels~~advection or vice versa, linked to regionally specific synoptic-scale circulation anomalies (ridge or ~~through-trough~~ patterns). These dominant effects of advection are modulated by changes in adiabatic and diabatic processes in the transported air parcels, which ~~tend to~~ either amplify or dampen DTDT decreases (~~cooling~~ld events) and increases (warming events) depending on the region and season. In contrast, ~~DTDT extremes~~Extreme DTDT changes during December-February in the tropics are controlled by local processes rather than changes in advection. For instance, the
20 most significant DTDT decreases are associated with a shift from less cloudy to more cloudy conditions, highlighting the crucial role of solar radiative heating. The mechanistic insights into extreme DTDT changes obtained in this study can help improve the prediction of such events and anticipate future changes in their occurrence frequency and intensity, which will be investigated in part II of this study.

1. Introduction

25 Day-to-day temperature (DTDT) ~~changes~~variations, here represented by temperature differences between consecutive days, can have significant implications across various sectors, including economic, ecology, and human health (Gough, 2008; Zhou et al., 2020; Kotz et al., 2021; Hovdahl, 2022). A change in DTDT ~~variability~~variation is linked to increased mortality rates, with the impact varying across geographic regions such as northern latitudes, tropics, and southern latitudes (Chan et al., 2012; Hovdahl, 2022; Sarmiento, 2023; Wu et al., 2022a). A recent study further reveals that ~~variations in~~
30 ~~temperature~~temperature changes ~~variability~~ can impact heat-related mortality by regionally up to more than 7% of total

deaths (Wu et al., 2022b). High DTD ~~variabilityvariation~~ has a negative effect on economic activity (Linsenmeier, 2023), with economic losses exhibiting regional disparities, as a 1°C increase in DTD ~~variabilitychange~~ results in an increase of 3-5% in vulnerability in mid and high-latitude areas but more than 10% in low-latitude and coastal regions (Kotz et al., 2021). These previous studies highlight the critical need for comprehensive studies investigating DTD ~~variabilityvariation~~ and the underlying atmospheric processes in the present climate.

With regard to long-term trends in DTD ~~variabilitychange~~, the early study by Karl et al. (1995) observed a decrease at mid-to-high latitude stations, particularly during the summer season, while no significant trend was detected in Australia. Recently, Xu et al. (2020) extended these ~~results by demonstrating a substantial increase in summer DTD results by demonstrating a substantial increase in summer DTD changevariability~~ across diverse regions such as the Arctic coast, South China, and Australia, but decreasing winter DTD ~~variabilitychange~~ in mid to high latitudes. These trends align with the comprehensive analysis by Krauskopf and Huth (2024) and Wan et al. (2021), ~~attributing spatiotemporal fluctuations in global variabilityvariationtemperature variability~~, except during boreal summer, to anthropogenic influences. Although most prior investigations have predominantly focused on analyzing trends in ~~the average magnitude of DTD variabilitychangeity~~, it is equally important to understand ~~DTD extremesextreme DTD changes~~. The concept of ~~a-extreme DTD-extreme~~ events, characterized by daily average temperature changes larger than $\pm 10^{\circ}\text{C}$, has been introduced in a recent study ~~that only focusing-focused~~ on mid-high latitudes (Zhou et al., 2020). Since higher DTD ~~variabilityvariation~~ is observed in the northern mid-high latitudes, spanning regions such as North Asia, the United States, and Europe (Gough, 2008; Xu et al., 2020), we can also expect more pronounced ~~DTD extremesextreme DTD changes~~ in these regions compared to lower latitudes (Figures ~~23a-d~~), which is consistent with the findings of (Zhou et al., 2020). Here, to account for such regional differences and investigate ~~DTD extremesextreme DTD changes~~ globally, we utilize percentile-based thresholds, as widely used for identifying temperature extremes (Bieli et al., 2015; Pfahl, 2014; Nygård et al., 2023~~a,b~~).

The relationship between ~~daily~~ temperature extremes (extremely high or low temperature, not ~~DTD extremesextreme DTD changes~~) and distinct circulation patterns at global and regional scales has been thoroughly investigated (Horton et al., 2015; Adams et al., 2021; Nygård et al., 2023~~a~~; Pfahl, 2014). ~~The daily temperature extremes and extreme DTD changes reveal similar circulation patterns, which are more pronounced in the case of daily temperature extremes (Figure S7e-h).~~ For example, in Europe, extreme warm events in summer often coincide with blocking anticyclones or subtropical ridges, while winter cold extremes are linked to North Atlantic blocking ~~(Figure S7f)~~, facilitating the intrusion of cold air masses (Nygård et al., 2023~~a~~; Kautz et al., 2022~~b~~; Pfahl and Wernli, 2012; Sillmann et al., 2011). Similarly, warm extremes in North America correlate with anticyclonic circulation and ridges, whereas extreme cold is linked to troughs and advection of continental air masses (Adams et al., 2021; Wang et al., 2019). ~~Such development and movement of cyclones and anticyclones drive the formation of frontal structures, which are k~~Key drivers of DTD variability are frontal structures (Ghil and Lucarini, 2020), ~~and have been extensively studied andthe relevance of fronts confirmed for European DTD~~

65 ~~extremes using various frontal structures~~has been confirmed in the detailed study by (Piskala and Huth, (2020). Further,
pParticular insights into the ~~associated~~ physical processes associated with daily temperature extremes have been obtained
from Lagrangian studies based on air parcel trajectory analyses, which have quantified the contributions of advection,
adiabatic, and diabatic ~~heating/cooling~~ warming/cooling to temperature extremes (Schumacher et al., 2019; Bieli et al., 2015;
Röthlisberger and Papritz, 2023b, a; Zschenderlein et al., 2019; Hartig et al., 2023). All these studies highlight the
70 significance of specific circulation anomalies for causing extreme weather in mid-to-high latitudes. In contrast, tropical
regions typically exhibit weaker temperature advection. However, an accelerated warming of extreme temperatures across
tropical land has been observed recently (Byrne, 2021). These changes can be linked to shifts in wind patterns, precipitation,
radiation, cloud cover, and surface fluxes (Gough, 2008; Matuszko et al., 2004; Sun and Mahrt, 1995; Dirmeyer et al., 2022).
These previous studies have established ~~the groundwork~~groundwork for understanding the origins of daily temperature
75 extremes, providing a fundamental basis also for deeper investigations into ~~DTDT-extremes~~extreme DTDT changes globally.

This paper investigates in detail the influence of altering air mass properties within the large-scale atmospheric circulation on
~~the variability~~variation of DTDT-extremesextreme DTDT changes. We use observations and reanalysis data to quantify the
magnitude of ~~DTDT-extremes~~extreme DTDT changes worldwide. To study the underlying processes, we apply a composite
80 approach and perform a Lagrangian analysis, calculating backward trajectories of surface air masses from selected locations
on the two days involved in ~~DTDT-extremes~~extreme DTDT changes. The contributions of temperature advection, adiabatic,
and diabatic ~~processes~~ warming are then quantified following previous studies of temperature extremes (Bieli et al., 2015;
Röthlisberger and Papritz, 2023a; Santos et al., 2015; Röthlisberger and Papritz, 2023b; Nygård et al., 2023~~a~~). We aim to
address the following research questions: (1) Which (changes in) atmospheric circulation patterns occur on consecutive days
85 associated with ~~DTDT-extremes~~extreme DTDT changes? (2) Which physical processes contribute to the occurrences of
~~DTDT-extremes~~extreme DTDT changes?

2. Data and Method

2.1 Observations

HadGHCND is a gridded daily temperature data set that includes near-surface minimum and maximum temperature data from 1950 to the present, developed by the National Centers for Environmental Information. It is based on meticulously quality-controlled observations from 27,000 global stations within the Global Historical Climatology Network daily database (Caesar et al., 2006). The data have been interpolated on a 2.5° latitude by 3.75° longitude grid, employing an angular distance weighting scheme for spatial consistency. Specifically designed to analyze climate extremes and climate model evaluation, the dataset offers temperature anomalies (based on a 1961–1990 climatology) and actual temperatures separately. Given its comprehensive nature and rigorous quality control, the HadGHCND data provides a robust foundation for global climatic studies (Xu et al., 2020; Wan et al., 2021). For the current study, we have used global daily HadGHCND (minimum (TN) and maximum (TX)) temperature from 1980 to 2014 and then calculated the daily mean temperature. (Rohde and Hausfather, 2020)(Rantanen et al., 2022; Russo and Domeisen, 2023)

2.1.2 ERA5 Reanalysis data

ERA5 is the fifth-generation European Centre for Medium-Range Weather Forecasts (ECMWF) global reanalysis product, providing climate and weather data for the past eight decades. It was developed by 4D-Var data assimilation in cycle CY41R2 of the ECMWF Integrated Forecasting System (Hersbach et al., 2020). It is an updated version of the widely used ERA-Interim reanalysis, employing a newer version of the ECMWF Earth system model with 137 hybrid sigma/pressure levels in the vertical up to 0.01 hPa (Hersbach, 2019). It provides hourly estimates of several atmospheric, ocean-wave, and land-surface quantities on a regular latitude-longitude grid of 0.25 degrees. Recently, ERA5 data has been used for different climate and weather-related global and regional studies (Böker et al., 2023; Simmons, 2022), and some have recommended it as the best alternative for regions with sparse observational coverage (Sharma et al., 2020; Sheridan et al., 2020). We use ERA5 data from 1980 to 2020, encompassing global daily mean 2m-surface air temperature (calculated from hourly temperature), total precipitation, and several three-dimensional atmospheric fields (temperature, horizontal and vertical winds, geopotential). The spatial resolution for all analyses is 0.25° × 0.25°, except for the trajectory calculations, for which input data at a horizontal resolution of 0.5° × 0.5° are employed. The temporal resolution of the near-surface temperature and composite analysis is daily, while the input data for the trajectories ~~have~~ has an hourly ~~resolution~~ resolution. We have compared the magnitude of DTD changes from ERA5 data with observational datasets (HadGHCND and Berkeley Earth Surface Temperatures (BEST)), with a detailed description of the datasets available in the supplementary material.

2.2.3 DTD ~~variability~~ variation and extremes

This study defines DTD change, denoted as δ_T , as the difference in daily mean near-surface air temperature between the previous day (T_{t-1}) and the day of the event (T_t), as shown in Eq. (1).

$$\delta_T = (T_t - T_{t-1}) \quad (1)$$

The average daily temperature change, μ_{DTDT} reflects the difference between the temperatures at the start (T_0) and end (T_n) of the time series (Eq. 2).

$$\mu_{\text{DTDT}} = \frac{1}{n} \sum_{t=1}^n (T_t - T_{t-1}) = \frac{T_n - T_0}{n} \quad (2)$$

To capture typical DTDT changes, we thus use the standard deviation, σ_{DTDT} , as shown in Eq. (3).

$$\sigma_{\text{DTDT}}^2 = \frac{1}{n} \sum_{t=1}^n (T_t - T_{t-1})^2 \quad (3)$$

By inserting the average daily temperature μ_T and multiplying out the square bracket, we find a relationship between σ_{DTDT} , the standard deviation of the daily mean temperature (σ_T) and the covariance between consecutive days ($\text{COV}(T_t, T_{t-1})$):

$$\begin{aligned} \sigma_{\text{DTDT}}^2 &= \frac{1}{n} \sum_{t=1}^n ((T_t - \mu_T) - (T_{t-1} - \mu_T))^2 \\ &= \frac{1}{n} \sum_{t=1}^n ((T_t - \mu_T)^2 + (T_{t-1} - \mu_T)^2 - 2(T_t - \mu_T)(T_{t-1} - \mu_T)) \\ &\approx 2\sigma_T^2 - 2\text{COV}(T_t, T_{t-1}) \quad (4) \end{aligned}$$

The approximation in equation (4) is associated with the fact that, for large n , both $\frac{1}{n} \sum_{t=1}^n (T_{t-1} - \mu_T)^2$ and $\frac{1}{n} \sum_{t=1}^n (T_t - \mu_T)^2$ are good estimators of σ_T^2 . Finally, the standard deviation of DTDT can thus be expressed as a function of the usual standard deviation (σ_T) and the lag-1 autocorrelation ($r_{1,T}$) of daily mean temperature, as shown in Eq. (5).

$$\sigma_{\text{DTDT}} = \sigma_T \sqrt{2(1 - r_{1,T})} \quad (5)$$

This study defines the DTDT change, δT , as the difference in daily mean near-surface air temperature between the previous ($t-1$) and events day (t), as shown in Eq. (1).

$$\delta T = (T_t - T_{t-1}) \quad (1)$$

$$\mu_T = \frac{1}{n} \sum_{t=1}^n (T_t - T_{t-1}) = \frac{T_n - T_0}{n} \quad (2)$$

$$\sigma_{\text{DTDT}}^2 = \frac{1}{n} \sum_{t=1}^n (T_t - T_{t-1})^2 \quad (3)$$

$$\begin{aligned} &= \frac{1}{n} \sum_{t=1}^n ((T_t - \mu_T) - (T_{t-1} - \mu_T))^2 \\ &= \frac{1}{n} \sum_{t=1}^n ((T_t - \mu_T)^2 + (T_{t-1} - \mu_T)^2 - 2(T_t - \mu_T)(T_{t-1} - \mu_T)) \\ &\approx 2\sigma_T^2 - 2\text{COV}(T_t, T_{t-1}) \end{aligned}$$

$$\sigma_{\text{DTDT}} = \sigma_T \sqrt{2(1 - \text{ACORR}(T_t, T_{t-1}))} \quad (4)$$

$$\sigma_{\text{DTDT}} = \sigma_T \sqrt{2(1 - r_{1,T})} \quad (5)$$

Given that T_t and T_{t-1} are the near surface air temperature on the event and previous day. The average over these daily changes, μ_T , only reflects the difference between the daily temperature at the beginning and end of the time series (Eq. 2), we use their standard deviation σ_{DTDT} to quantify typical DTDT changes. This standard deviation can be expressed as a

function of the usual standard deviation σ_T and the lag-1 autocorrelation $r_{1,T}$ of daily mean temperature, as shown in Eq. (5):

In addition, extreme DTDT changes are studied using the percentile method. ~~Extreme cooling~~ and ~~warming~~ ~~extreme DTDT change~~ ~~changes event~~ ~~events~~ at each grid point are identified using the 5th and 95th percentiles of the DTDT change ~~distribution~~ as thresholds, ~~respectively~~. The analyses focus on the two main seasons: December-February (DJF) and July-August (JJA). Accordingly, 184 events in DJF and 188 events in JJA are selected at each location ~~based on the ERA5 dataset~~.

2.34 Trajectory setup

The Lagrangian analysis tool (LAGRANTO), introduced by Sprenger and Wernli (2015), is used to calculate backward trajectories of near-surface air masses on days associated with extreme DTDT changes from 1980 to 2020. The trajectories are initialized at 18 UTC on both the preceding day ($t-1$) and on the event day (t) at 10, 30, 50, and 100 hPa above the surface at the corresponding grid cells. Similar to previous studies of extreme temperatures (Zschenderlein et al., 2019), the different initialization heights are used to sample a near-surface layer that is assumed to be well-mixed. The time difference of 24 hours between the two initializations allows for a proper separation of the air masses before and after the temperature change. Although LAGRANTO is used to calculate 10-day backward trajectories, extremes typically develop on a timescale of 2–3 day (Bieli et al., 2015; Röthlisberger and Papritz, 2023a). Therefore, we focus on 3-day backward trajectories for the analysis. Various variables of interest, including latitude, longitude, pressure, temperature, and potential temperature, are interpolated along the trajectory paths and saved at 1-hour intervals.

The Lagrangian analysis tool (LAGRANTO) introduced by Sprenger and Wernli (2015) is employed to calculate backward trajectories of near surface air masses on the days involved in an extreme DTDT change events. The trajectories are initialized at 18 UTC on both days and at 10, 30, 50, and 100 hPa above the surface at the corresponding grid points. Various variables of interest, including latitude, longitude, pressure, temperature, and potential temperature, are interpolated along the trajectory paths and saved in 1 hour intervals. The initialization time of the trajectories in the following is referred to as $t=0$.

2.45 Lagrangian temperature variability decomposition

To better understand the underlying mechanisms of extreme DTDT changes, our analysis focuses on four specific locations: two grid points in the Northern Hemisphere mid-latitudes: (North America (52°N, 86°W) and Europe (50°N, 10°E)), one in tropical South America (13°S, 24°E), and another on the southern coast of Australia (37°S, 140°E). The results for a few additional grid points (Northern Asia (70°N, 90°E), Southern South America (37°S, 68°W), South Asia (23°N, 80°E), South Africa (13°S, 24°E), and Western North America (45°N, 120°W)) are presented in the supplementary material. At these

locations, we ~~apply~~introduce a novel Lagrangian temperature ~~variation~~ decomposition method to quantify contributions of advection, adiabatic, and diabatic processes to ~~extreme DTDT change extremes~~, similar to approaches used for near-surface hot and cold extremes (Röthlisberger and Papritz, 2023b, a). ~~This decomposition is applied to backward trajectories initiated on the two days (t-1 and t) involved in extreme DTDT changes, focusing on a 3-day Lagrangian time scale. The appendix presents a detailed derivation of the diagnostic, leading to the decomposition. This decomposition is applied to backward trajectories initiated on the two days involved in an extreme DTDT change events. A detailed derivation of the diagnostic is presented in the appendix. In summary, the Lagrangian decomposition of DTDT changes is obtained from, as approximated by computed the trajectories, and here evaluated on a 3-day Lagrangian time scale, and is evaluated here on a 3-day Lagrangian time scale, which is~~ given in Eq. (6).

$$\delta_T^0 \approx \delta_T^{-3d} + \delta_T^{\text{adi}} + \delta_T^{\text{dia}} + \text{res} \quad (6)$$

The DTDT change at the surface (δ_T^0) ~~has been~~ is decomposed into three contributing factors: the mean temperature difference at the origin of the air parcels, three days before initialization, ~~which~~ indicates the contribution of advection (δ_T^{-3d}). ~~When the original temperature of the air parcels was initialized on the previous day (\bar{T}_{t-1}^{-3d}) is higher than the original temperature of the air parcels initialized at the event (\bar{T}_t^{-3d}), this represents a shift from the advection of originally warmer air on the preceding day to colder air on the event day, which is referred to as cold air advection. The reverse is true for warm air advection. A further contributions come from~~ mean adiabatic ~~warming~~compression or ~~cooling~~-expansion resulting from vertical descent or ascent, respectively (δ_T^{adi}), and ~~a contribution of~~ mean diabatic heating or cooling from processes such as latent heating in clouds, radiation, ~~and~~ surface fluxes (δ_T^{dia}). Furthermore, ~~t~~The final term is the residuum (res), resulting from numerical inaccuracies in ~~derivative the~~ calculation ~~of derivatives~~. The residual is typically small and is thus not further discussed in the following text and the figures.

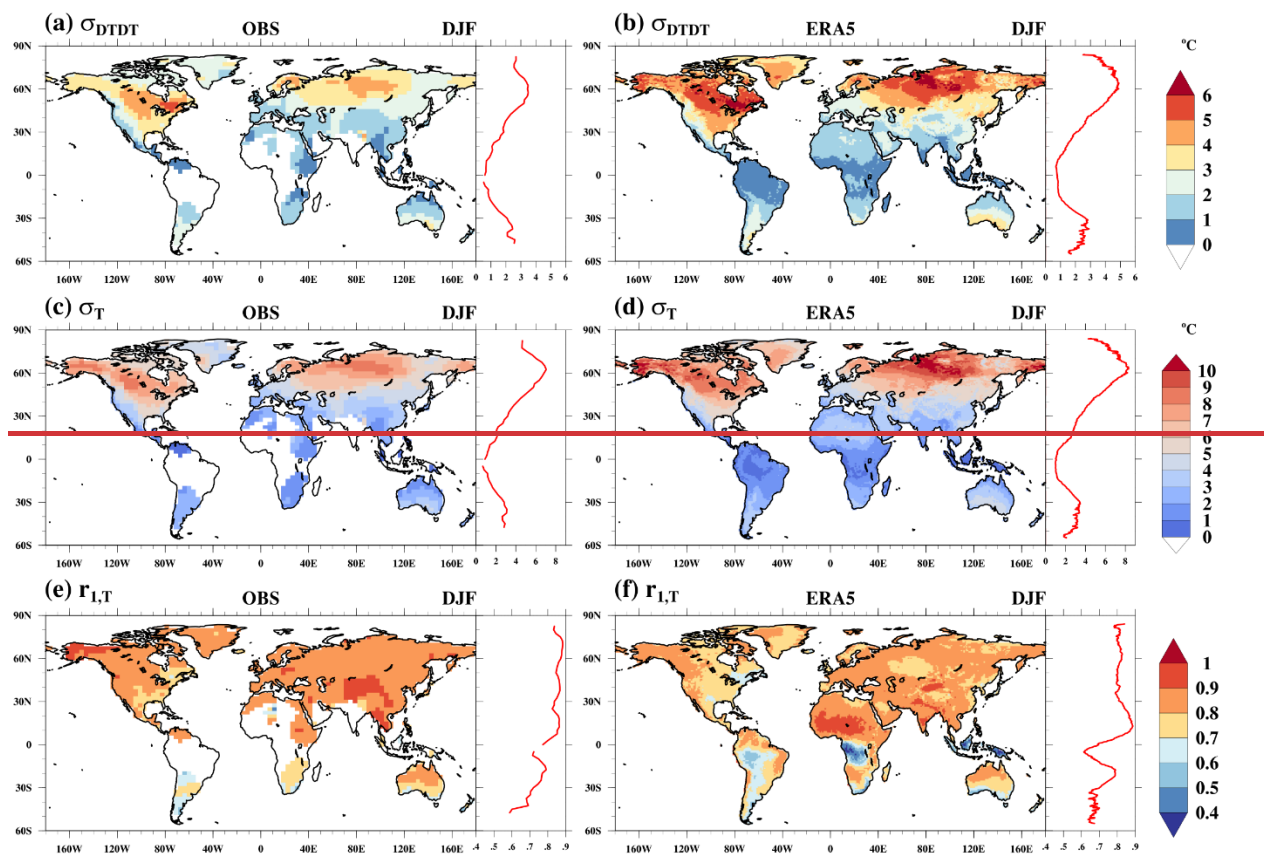
3. Result

3.1 DTDT variations in DJF and JJA

Both the ~~HadGHCND and ERA5~~ and Observations (HadGHCND and BEST) datasets reveal that the magnitude of DTDT ~~DTDT variations, quantified by $\sigma(\sigma_{\text{DTDT}})$ changes~~ is larger in the extratropics than in the tropics during DJF and JJA (Figures 1a-b and S12a-d, see zonal average plot as well). Notably, σ_{DTDT} ~~variability~~variation is larger during DJF than in JJA in the Northern Hemisphere, while the seasonal cycle is less clear in the ~~Southern~~Southern Hemisphere, with higher σ_{DTDT} in JJA in

Antarctica, central South America, South Africa, and northern Australia, but higher σ_{DTDT} in DJF in southern Australia (except in Antarctica). The magnitude of the seasonal differences is particularly evident in North America, the Northern Eurasian continent, and southern Australia. In DJF, the σ_{DTDT} variability is above 4°C in many regions (Figures 1a-b), compared to $1-4^{\circ}\text{C}$ during JJA (Figures 12a-bb). However, σ_{DTDT} variations remain consistently around $1-2^{\circ}\text{C}$ in the tropics and $\geq 1-2^{\circ}\text{C}$ over higher latitude land regions in the southern hemisphere (except southern Australia) during both seasons. Furthermore, the ERA5 dataset indicates a considerably larger magnitude of σ_{DTDT} changes than the observations (in particular mostly for HadGHCND), primarily in the mid-to-high latitudes of the northern and southern hemispheres. HadGHCND, primarily in northern hemisphere high latitudes and southern Australia. This may be related to deficiencies of the HadGHCND dataset, which may have smoothed out the variability due to spatial interpolation and the lack of adequate station coverage in these some regions (Fig. S1 of Wan et al. (2021)). However, σ_{DTDT} values from the variability pattern of ERA5 are more comparable to BEST, which incorporates additional data sources beyond HadGHCND (Rohde and Hausfather, 2020).

Since the magnitude of σ_{DTDT} changes can be expressed as a function of the standard deviation σ_T and lag-1 autocorrelation $r_{1,T}$ of daily mean temperature (see again Eq. 5), Figures 1c-f and 2 and S1e-l also show these related quantities and their respective zonal averages for DJF and JJA. While observations, HadGHCND and ERA5 mostly agree on the spatial pattern of σ_T , there is a slight overestimation of the magnitude of σ_T in ERA5 regionally during DJF (Figures 1c-d and S1e-h). This overestimation is more widespread and larger in JJA (Figures 2e-d). The spatial distribution of σ_T follows a pattern consistent with σ_{DTDT} , with generally higher variability values in northern hemisphere mid-high latitudes ($\geq 4-5^{\circ}\text{C}$ in DJF and $2-6^{\circ}\text{C}$ in JJA) and southern hemisphere extratropics ($2-8^{\circ}\text{C}$ in both seasons). In comparison, the tropics exhibit smaller σ_T variability (1- 4°C in DJF and JJA) of σ_T .



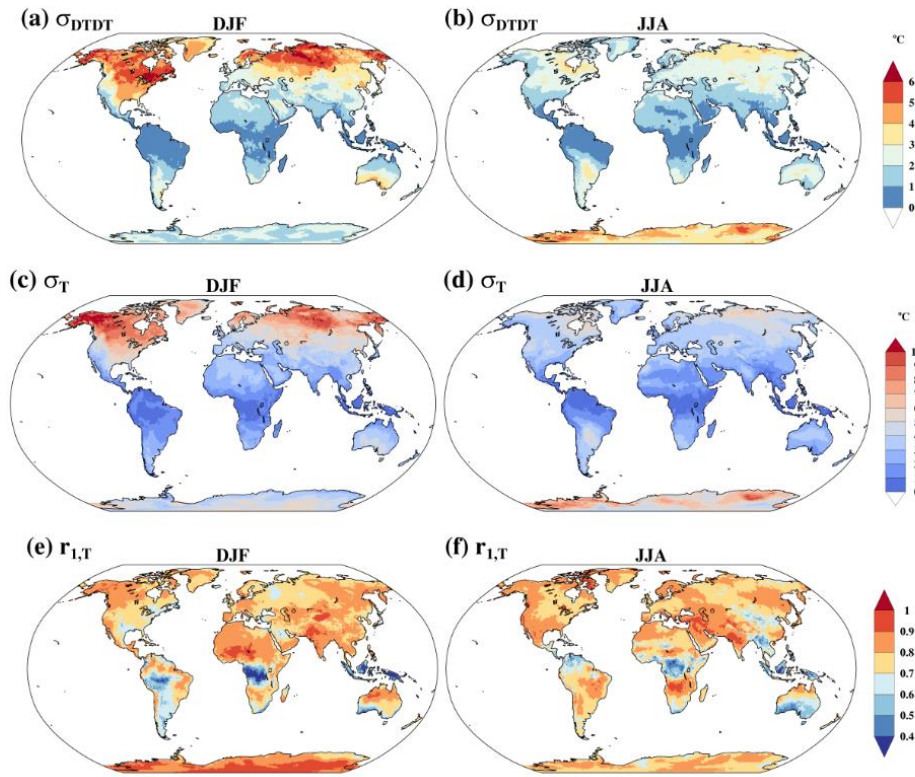


Figure 14. (a, b) Standard deviation of DTD variations (σ_{DTD} , °C), (c, d) standard deviation of daily mean temperature (σ_T , °C), and (e, f) lag-1 autocorrelation of daily mean temperature ($r_{1,T}$) in December-February (DJF, 1st column) and June-August (JJA, 2nd column), derived from the the HadGHCND (1st column) and ERA5 (2nd column) datasets. The zonal average of the σ_{DTD} , σ_T , and $r_{1,T}$ are attached to each plot.

In HadGHCND, the autocorrelation is spatially rather homogeneous, while there are more pronounced spatial variations with generally lower correlations in the BEST and ERA5 datasets (Figures 1e-f and S1i2e-1f). Autocorrelation values are typically below 0.8 (and locally below 0.6) in the deep tropics, eastern North America, the southern hemisphere land regions south of approximately 30°S, and the eastern half of the Asian continent in JJA, and above 0.8 in other regions.

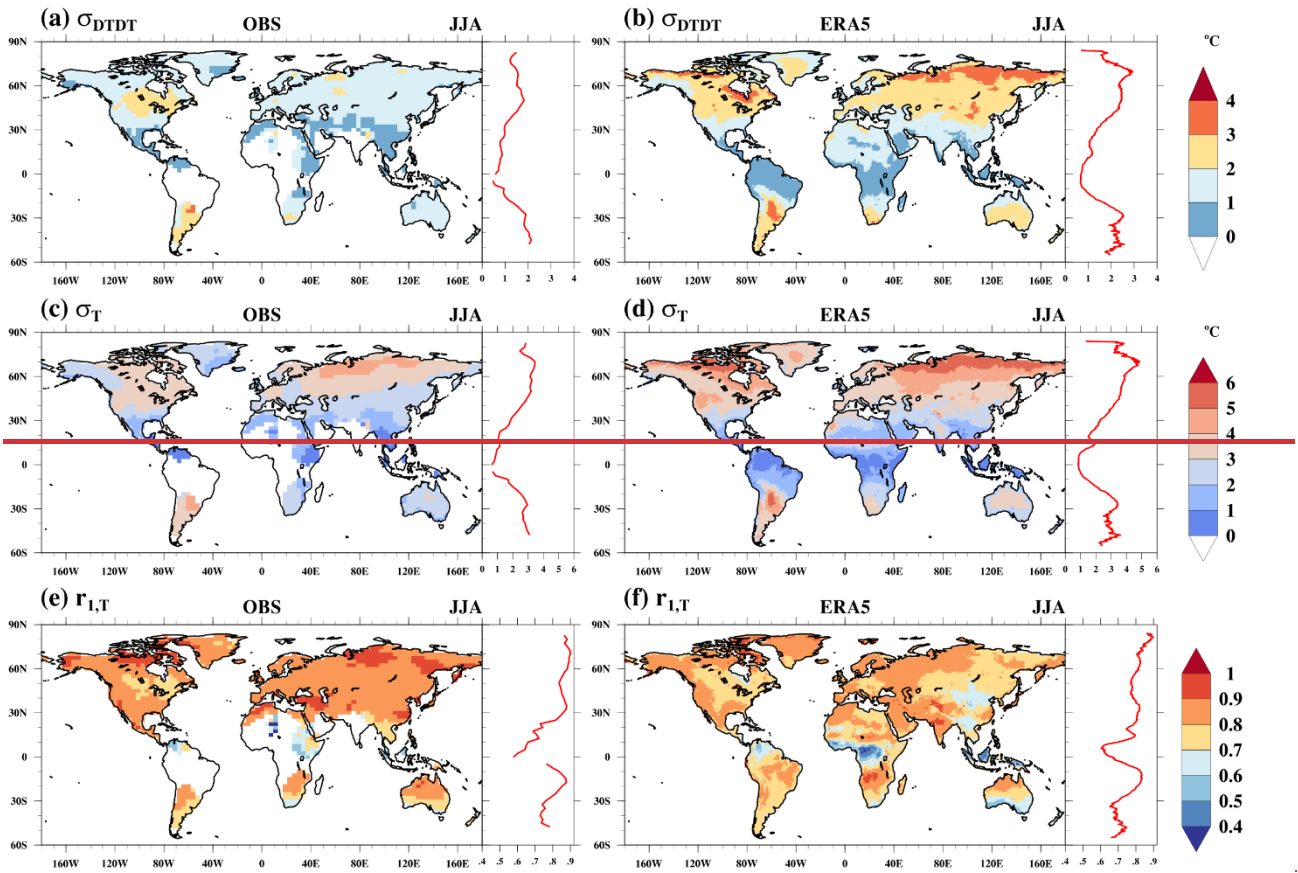


Figure 2. (a, b) Standard deviation of DTD variations (σ_{DTD} , °C), (c, d) standard deviation of daily mean temperature (σ_T , °C), and (e, f) lag-1 autocorrelation of daily mean temperature ($r_{1,T}$) in June-August (JJA) derived from the HadGHCND (1st column) and ERA5 (2nd column) datasets. The zonal average of the σ_{DTD} , σ_T , and $r_{1,T}$ are attached to each plot.

Comparing the global patterns of σ_{DTD} , σ_T , and $r_{1,T}$ shows that the spatial ~~variability~~ variation of σ_{DTD} is mostly determined by variations in σ_T . A high standard deviation σ_T is typically associated with ~~leads to typically~~ large σ_{DTD} ~~changes~~ in higher latitudes, despite a ~~relative-relatively~~ high $r_{1,T}$ (see again Eq. 5), while in the tropics, σ_{DTD} is ~~lower~~ smaller associated with lower σ_T , despite lower $r_{1,T}$. Nevertheless, $r_{1,T}$ can affect the spatial pattern of ~~the~~ σ_{DTD} regionally. For instance, the north-south gradient of $r_{1,T}$ over Australia in JJA leads to larger σ_{DTD} ~~changes~~ in the south despite relatively homogeneous σ_T . With regard to the differences between ~~oObservationsHadGHCND~~ and ERA5, both a higher σ_T and lower $r_{1,T}$ in ERA5 contribute to the typically larger σ_{DTD} ~~changes~~ in the reanalysis data.

To gain detailed insights into the statistical distributions of DTD changes, Figure S2 shows such distributions for we selected various global locations around the globe—North America, Europe, South America, and Australia—and analyzed

the DTDT distribution during the DJF and JJA, as shown in Figure S2. In DJF, North America exhibits the highest variability of DTDT changes with a broad distribution, whereas South America shows the lowest variability with a more pronounced peak (Figure S2a). Europe and Australia display experience moderate variability, characterized by intermediate kurtosis values, and a slight distribution asymmetry (skewness) of the distribution for Australia. However, in JJA, South America becomes more variable, while North America, Europe, and Australia maintain relatively stable distributions with experience lower variability than in DJF (Figure S2b), consistent with the seasonal differences of σ_{DTDT} discussed above. Additionally, the distributions become more negatively skewed in JJA.

3.2 Extreme DTDT changes extremes

To investigate extreme DTDT changes, we use the 5th and 95th percentiles as thresholds at each grid point, as illustrated in Figures 23a-d. The spatial patterns of extreme DTDT changes, both warming and cooling, closely resemble those of σ_{DTDT} and σ_T , with higher values in the extratropics and lower values in the tropics (Figures Figure 1, 2, and 3). This similarity suggests that regions with greater DTDT variability variations are more prone to extreme DTDT changes events. Furthermore, extreme DTDT events are more intense (i.e., exhibit a larger magnitude) during DJF than JJA, particularly in the Northern Hemisphere. In contrast, the tropics display almost equal magnitudes of extreme DTDT changes in both seasons. The following section describes the atmospheric circulation and physical processes (according to Eq. 6) related to extreme DTDT events at selected global locations.

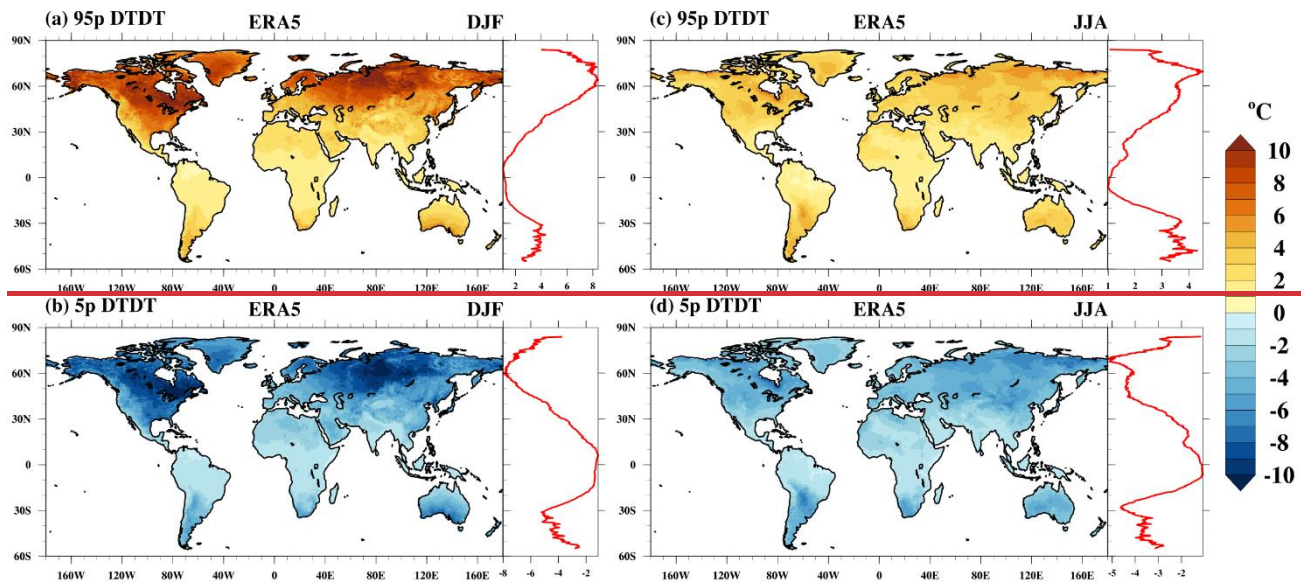
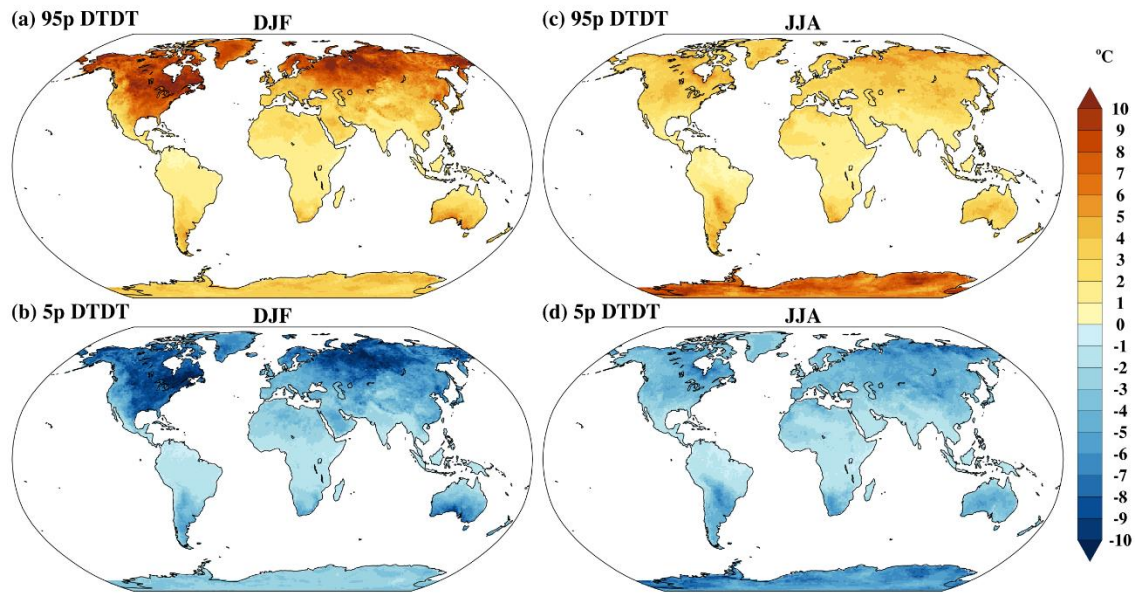


Figure 23. The (a, c) 95th percentile (95p) and (b, d) 5th percentile (5p) of DTD T ~~variations~~ changes during (a, b) December-February (DJF, 1st column) and (c, d) July-August (JJA, 2nd column) as derived from the ERA5 dataset. The zonal average of the 95p and 5p of DTD T changes are attached to each plot.

Furthermore, to investigate how DTD T changes relate to the daily temperature of the involved consecutive days, we analyzed the relationship between DTD T changes and specific quantiles (terciles) of T_t and T_{t-1} , as shown in Figure 3 for North America. Note that ~~similar patterns have been~~ are observed across other grid points (not shown); ~~therefore, we~~

present results specifically for North America for clarity. Our analysis reveals that extreme warming events typically originate in the lower to middle quantiles of T_{t-1} and shift toward the middle to higher quantiles of T_t . Conversely, extreme cooling events emerge from the middle to higher quantiles of T_{t-1} and transition to the middle to lower quantiles of T_t . Notably, we observe that extreme DTDT changes. The daily temperatures involved in extreme DTDT changes are thus not necessarily extreme, but typically occur when T_t predominantly falls within the tail quantiles. The following section examines the atmospheric circulation patterns and physical processes (as described in Eq. 6) associated with extreme DTDT events at the selected global locations.

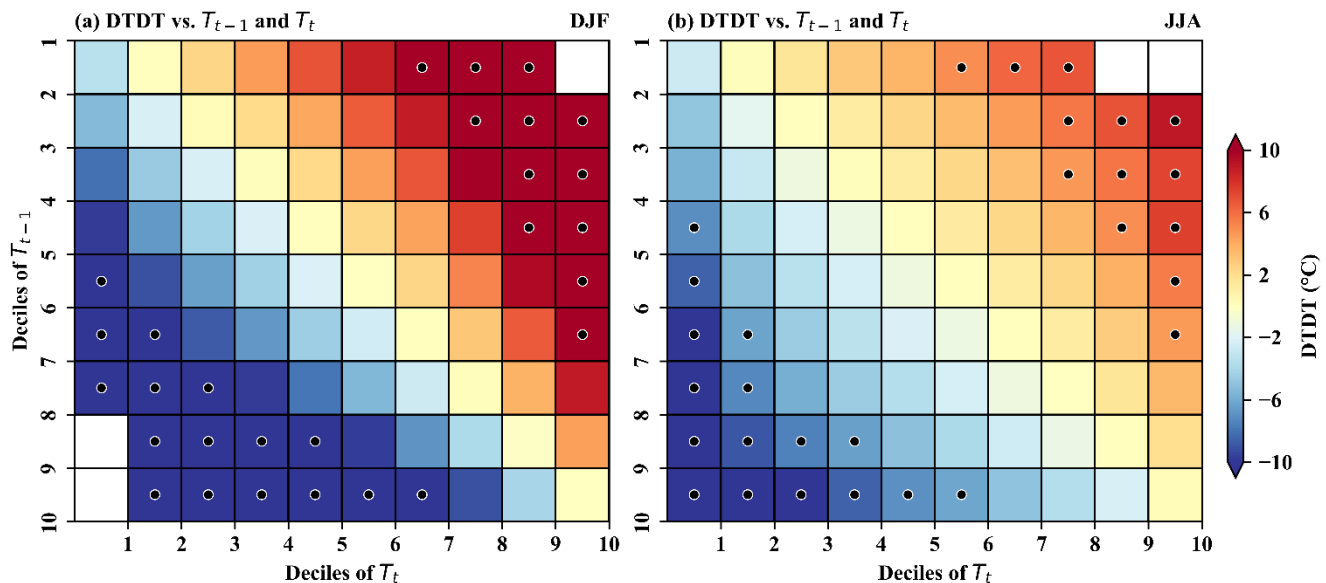


Figure 3. Heatmaps of the relationship between DTDT change and the deciles of temperature on the previous day (T_{t-1}) and the event day (T_t) for (a) December (DJF) and (b) June-August (JJA) for North America. The x-axis and y-axis represent deciles of T_t and T_{t-1} , while the color shading indicates DTDT changes, with red and blue colors indicating warming and cooling, respectively. The black circles represent extreme DTDT changes.

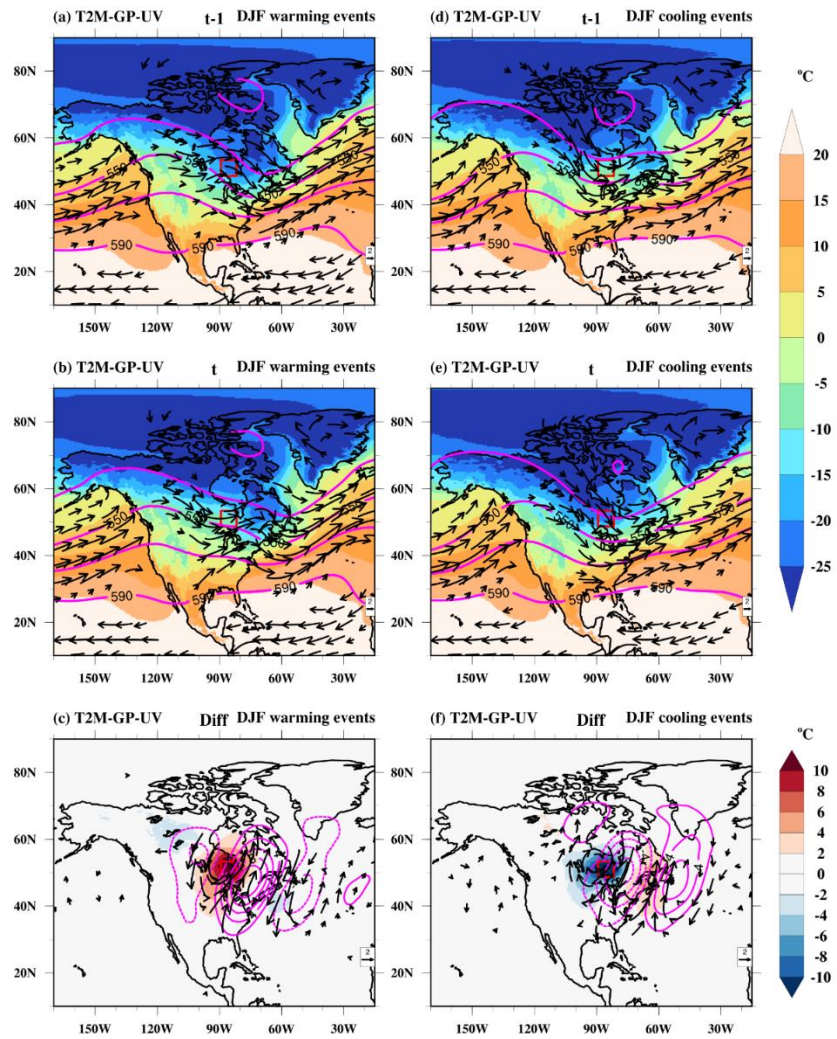
3.2.1 Mid-latitudes: North America

To explore the mechanism behind extreme DTDT changes in the mid-latitudes, we focus on a specific grid point in North America (52°N and 85°W), which is also representative of other North American regions (compare results with Fig. S52).

The synoptic-scale circulation patterns associated with DJF ~~warm events~~ warming events (exceeding the 95th percentile of DTDT changes) on consecutive days ~~and their differences are first analyzed using~~ are first analyzed with the help of composites, as shown in Figures 4a-fb. On the day preceding the events (t-1), a ~~distinct near-surface temperature~~ near-surface ~~temperature~~ dipole is observed across northern North America, with higher temperatures in the west ($\geq -10^{\circ}\text{C}$) and lower temperatures ($\leq -15^{\circ}\text{C}$) in the east and the vicinity of the selected location (Figure 4a). This temperature pattern is influenced by a ridge over the western part ~~facilitating warm, southerly airflow around its western flank and a trough over the eastern part of the continent, which facilitates warm~~ southerly winds around its western flank, and a trough over the eastern part of the continent, associated with cold ~~northerly winds associated with northerly~~ (Fig. S3a) ~~flow and cold air advection~~. This synoptic pattern aligns with the distribution of backward trajectories, indicating the advection of cold air masses from the Arctic region (Figure 5a). Over the 3d leading up to this preceding day, these cold air masses (mean temperature of -21.5°C at -3d) experience a gradual temperature increase (of 5.7°C), with significant adiabatic warming (8.3°C in the mean) due to a distinct 100hPa mean descent (Figures 5e-f). Limited diabatic ~~cooling~~ heating ~~cooling~~, likely due to longwave radiation, is indicated by a reduction in θ (by -2.6°C in the mean), constraining the temperature increase (Figure 5g). ~~Note that the residual is below 1°C (all locations), attributable to numerical inaccuracies in the computation of derivatives, which is negligible.~~ Accordingly, the temperature at t-1 is mainly determined by the cold air advection of cold, Arctic air masses, whose temperature increases due to mitigated by ~~adiabatic warming, with that overcompensates a slight~~ cooling ~~processes contributing to some additional decrease~~ cooling.

On the days of the DJF ~~warm events~~ warming events (t), the near-surface temperature reaches $\geq -10^{\circ}\text{C}$ on average, marking a notable increase compared to ~~the~~ t-1 (Figure 4b-c). This rise is attributed to an eastward extension of the ridge, displacing the preceding trough ~~arm~~ further to the east, which leads to ~~a~~ southwesterly ~~wind~~ advection anomalies at the selected location (Fig. S3b). The air parcel density shifts substantially southward compared to t-1, with the largest density southwest of the chosen location ($40\text{--}50^{\circ}\text{N}$, Figure 5b). This shift is associated with a substantially higher temperature 3d before arrival (-13.4°C in the mean) compared to the air parcels at t-1. The air parcels experience a vertical descent of 76hPa in the mean (Figure 5e), leading to adiabatic warming (6.7°C) and a general temperature increase in the 3d leading up to the events (Figure 5f). The net diabatic heating contribution is close to zero (0.4°C over 3d) but becomes more prominent in the last hours before the events, reaching 1.2°C in 24h (Figure 5g). Similar to t-1, the initially colder air masses are thus warmed on their way to the target location. Evaluating the differences in the physical processes between the two successive days (Eq. 6) reveals that changes in advection, associated with the shift in the air mass origin and initial temperature, are the ~~main leading~~ main leading cause for the local DTDT warming at the selected location, ~~contributing 8.1°C~~ contributing to 8.1°C ~~C~~ on average (Figure 5k). Reduced adiabatic warming (-1.6°C) due to a less pronounced descent on the day of the events counteracts the overall temperature increase, while ~~reduced~~ increased diabatic ~~heating~~ cooling (-3°C) provides another positive contribution. This diabatic contribution is associated with the largest events ~~s-to-events~~ variability variation (boxes and whiskers in Figure. 5k).

350 ~~Warm events~~ Warming events in JJA resemble those of DJF, including their atmospheric circulation patterns (not shown) and air parcel density distribution (Figs. S44a-b). The air parcels also experience similar adiabatic warming before arriving at the target location as in DJF, whereas the diabatic changes have a larger daily cycle and a stronger positive contribution on the last day (Figs. S44e-g). The DTDT warming, as in DJF, is mainly due to the change in the air parcels' initial temperature (0.9°C at t-1 and 6.4°C at t) and thus changes in advection (Fig. S44k). Mean contributions from adiabatic ~~warm~~ warming (1.9°C) and diabatic ~~heating~~ heating (0.8°C) are smaller in magnitude and flip signs compared to DJF ~~magnitude and flip signs compared to DJF~~.



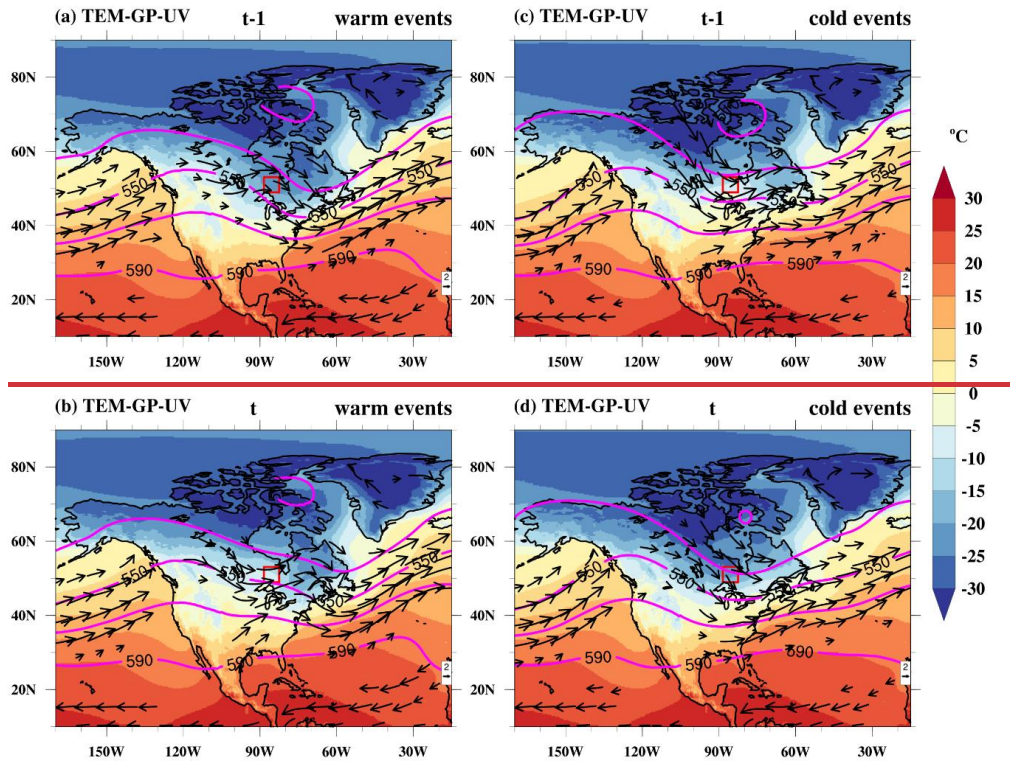


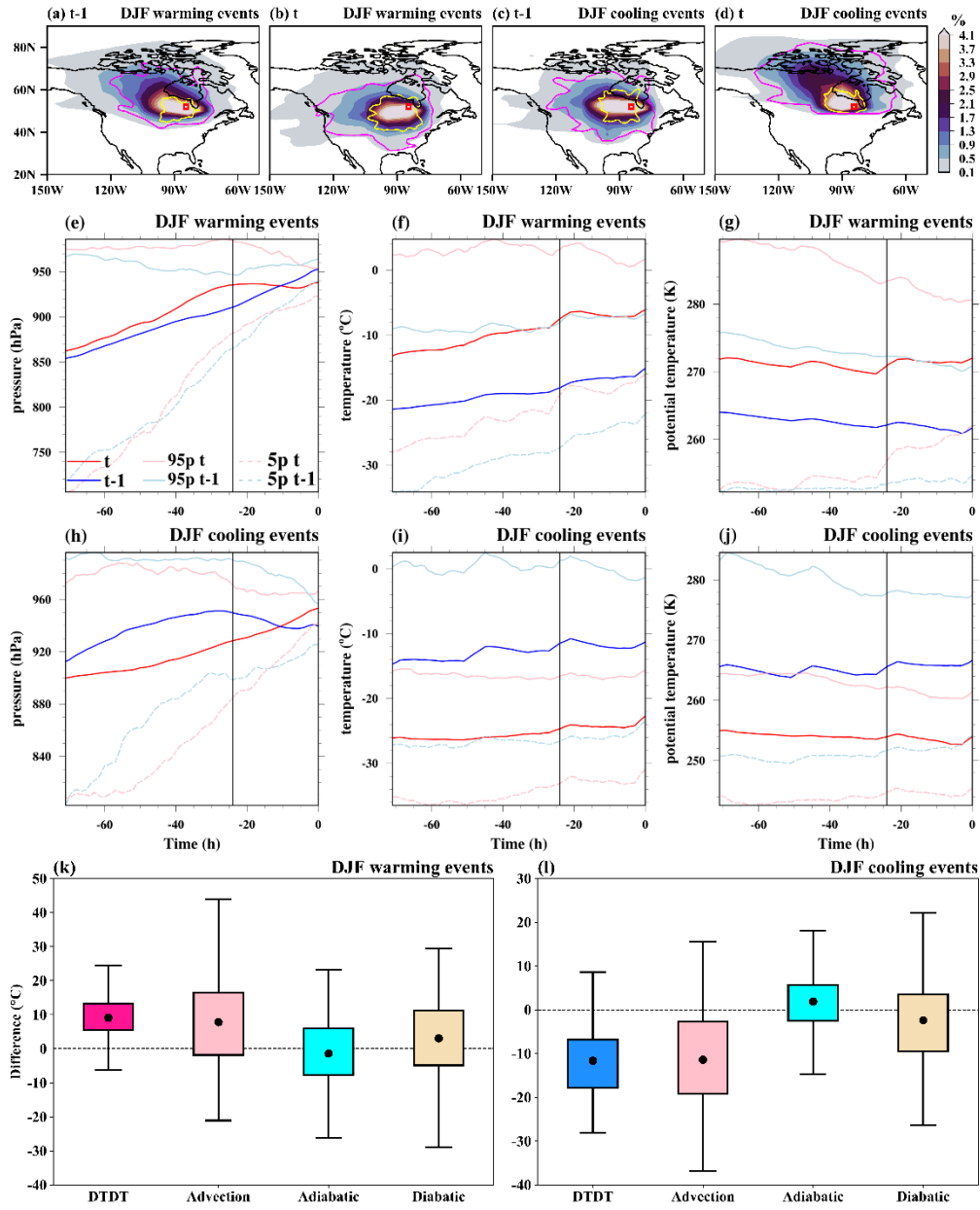
Figure 44. Composite of near-surface temperature (T2M, °C, color shading), wind at 850 hPa (UV, m/s, vectors), and geopotential height at 500 hPa (GP, gpm, magenta contours) on the (a, d) previous day (t-1), (b, e) event day (t) and (c, f) difference (diff) of event day and previous day of the warming (a-c) and cooling (d-f) events during December-February (DJF) at a selected grid point in North America (red box). Note that (in a-b and d-e) wind vectors ≥ 5 m/s and (in c, f) wind anomalies ≥ 1 m/s are plotted. The dotted and bold magenta contour in c and f indicates negative and positive geopotential height differences, respectively. Composite of near-surface temperature (TEM, °C, color shading), wind at 850 hPa (UV, m/s, vectors), and Geopotential height at 500 hPa (GP, gpm, magenta contours) on the (a, c) previous day (t-1) and (b, d) event day (t) of the warm (a,b) and cold events (c,d) during December-February (DJF) at a selected grid point in North America (red box). Note that wind vectors ≥ 5 m/s are plotted.

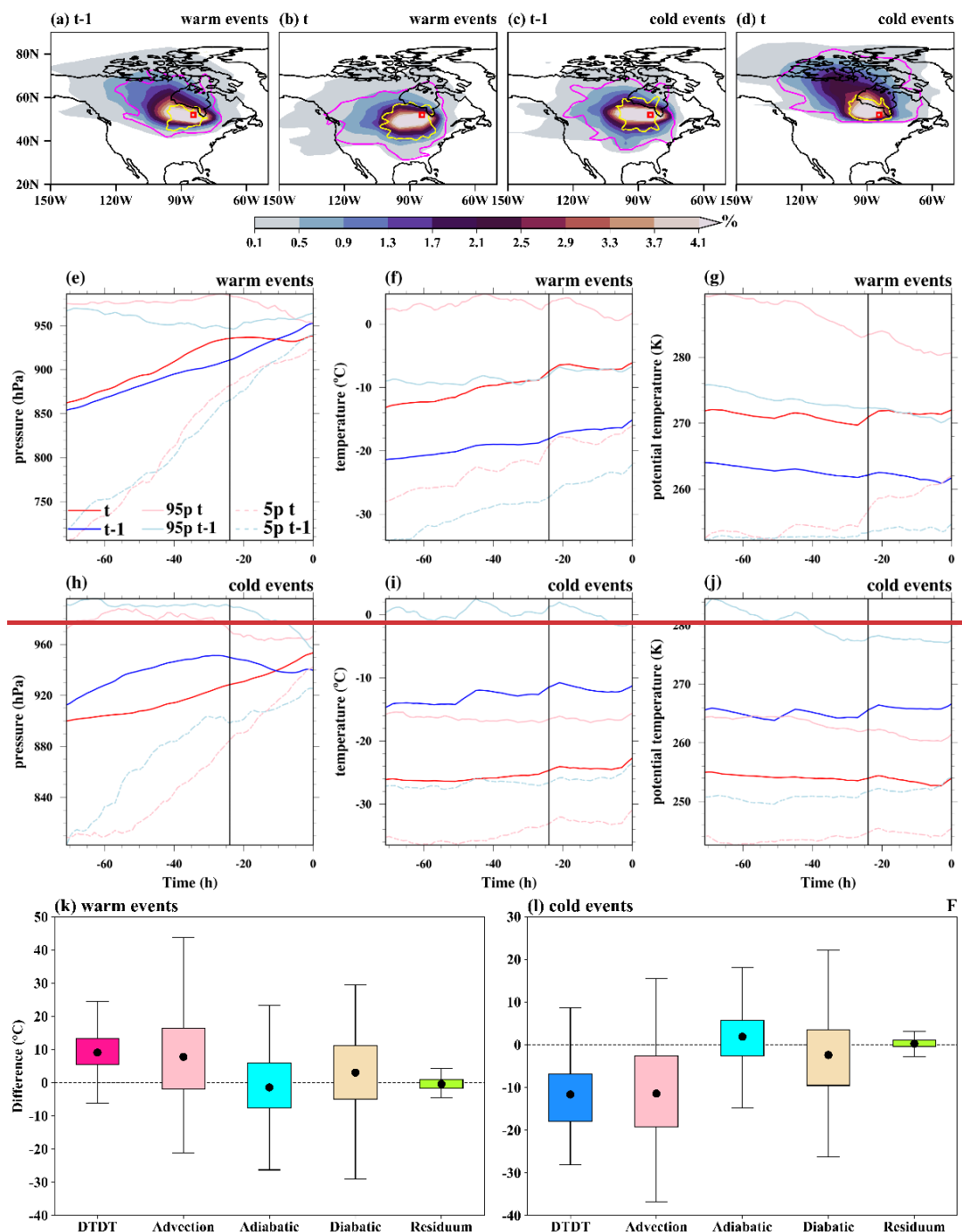
On the days preceding DJF ~~cold events~~ cooling events (t-1), there is a pronounced meridional temperature gradient in the region of the selected location, with near-surface temperature over the northern Arctic land region below -15°C , while milder temperatures ($\geq -10^{\circ}\text{C}$) prevail at the grid point and to its south (Figure 4de). This thermal gradient is linked to a trough over the Arctic juxtaposed with a ridge structure to its west. ~~Southwesterly~~ Westerly winds facilitate the transport of relatively warm air masses ~~from the west~~ towards the location (Figure 5e Fig. S3c and Figure 5c). The transported air parcels, with a mean temperature of -15°C (at -3d), undergo a gradual descent, experiencing a modest temperature increase of about 3.7°C in 3d, attributed to the combined effects of adiabatic warming (2.4°C) and diabatic heating ~~warming~~ (1.3°C), as shown in Figures 5h-j. While the descent and adiabatic warming dominate between ~~-3d and -2d~~ -3d and -2d, the last day before arrival

is characterized by diabatic ~~heating warming~~ (θ increase by 2°C , Figure 5j). ~~As for the t-1 events, the near-surface temperature at the selected location is thus mainly determined by advection, with some additional warming due to diabatic heating and adiabatic warming processes.~~

On the day of the events (t), a southward shift of the Arctic trough is associated with a turn of the wind towards the north-northwest at the selected location (Figure 4e ~~ed~~ and Fig. S3d). This corresponds to the arrival of northerly air parcels with an initially extremely low temperature of -26.2°C in the mean (Figure 5d). These air parcels undergo a subsequent temperature increase of 3.2°C in 3d due to adiabatic warming (4.3°C), partly offset by radiative cooling (-1.1°C , Figures 5h-j). Accordingly, a shift to strong northerly cold advection (Figure 4f and 5d), associated with a mean temperature difference of -11.2°C between the air parcels at -3d, is the predominant contributor to the DTDT ~~cold events cooling events~~ (Figure 5l). This advective effect is counteracted by moderately increased adiabatic warming (1.9°C) and complemented by amplified diabatic ~~cooling~~ (-2.4°C), collectively shaping the DTDT change.

In JJA, the DTDT ~~cold events cooling events~~ are driven by very similar processes as the ~~cold events cooling events~~ during DJF (Fig. S4), ~~with a shift from westerly to northerly transport (Figs. S1e-d) leading to a mean temperature drop of -8.6°C due to advection. A shift from westerly to northerly transport (Figs. S4c-d) leads to a mean temperature drop of -8.6°C due to cold air advection (Figs. S4c-d and h-j), while changes in adiabatic and diabatic warming are very small. Mean changes in adiabatic and diabatic processes are very small between the two days, with larger event-to-event variation (Fig. S4l).~~





395 **Figure 5.** The spatial distribution of trajectories initiated on the previous day (t-1) and event day (t) for both December-February (DJF) **warm** **warming** and **cold** **events** **cooling** **events** over North America. In the top row, the color-shading illustrates the air parcel trajectory density (%) based on the position between **-5d** **5d** and 0d. The magenta and yellow contours represent 0.5%

particle density fields at ~~—3d and 1d~~ -3d and -1d, respectively. The red box shows the selected grid ~~point~~ point over North America. The Lagrangian evolution of distinct physical parameters (pressure, temperature, potential temperature) along the air parcel trajectories for both warming (2nd-row) and ~~cold events~~ cooling events (3rd row) is presented in panels e-j. Panels k and l show the contribution of the different physical processes to the genesis of ~~DTDT extremes~~ extreme DTDT changes according to Eq. (6), which refers to a 3d-time scale. ~~The residuum is attributable to numerical inaccuracies in the computation of derivatives in Eq. (6).~~ The box spans the 25th and 75th percentiles of the data; the black dot inside the box gives the mean of the related quantities, and 1.5 times the interquartile range is indicated by the whiskers.

3.2.2 Mid-latitudes: Europe

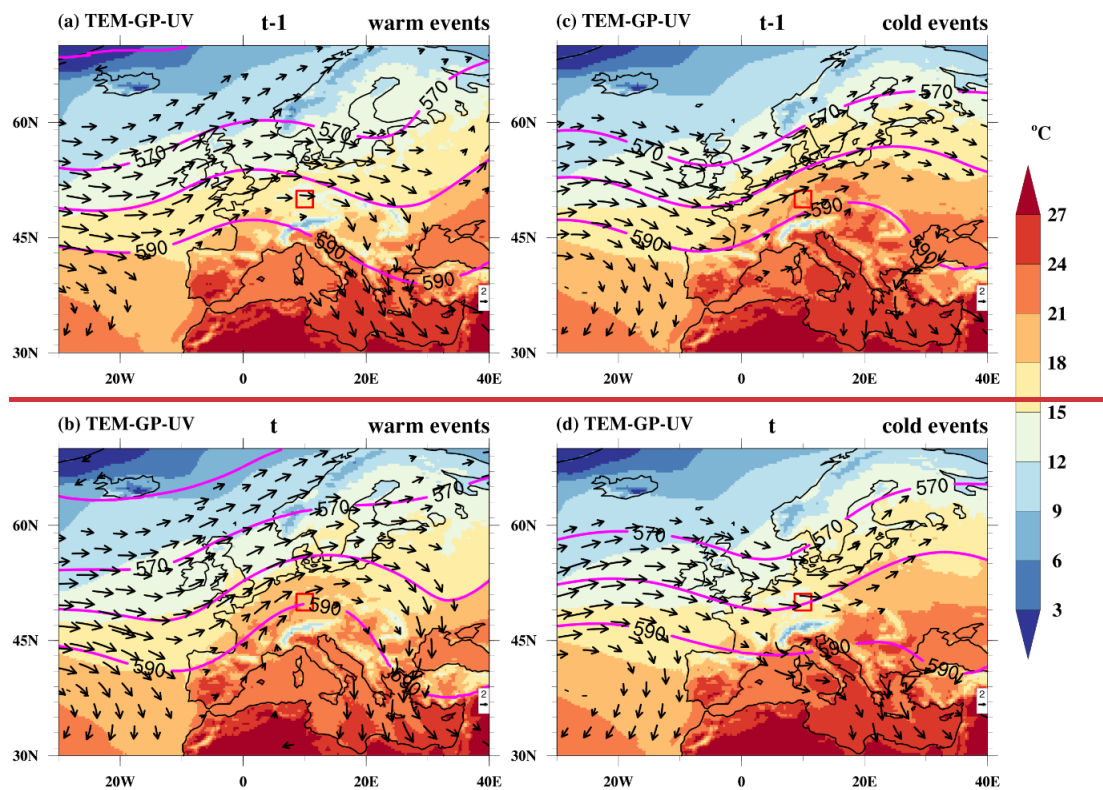
Another mid-latitude location where we investigate the mechanism driving extreme DTDT variations is a grid point over Europe (~~50°N and 10°E~~). This section focuses on the JJA season since the DJF events, ~~which are only briefly discussed~~, exhibit similarities with the location in North America studied in section 3.2.1.

During the preceding day of the JJA ~~warm events~~ warming events (t-1), the composite geopotential height pattern features a weak trough over the eastern North Atlantic and a developing ridge over Central Europe (Figure 6a). In this situation, the northern part of Central Europe, including the selected location, is under the influence of westerlies (~~Fig. S6a~~), transporting cool, maritime air masses towards the continent (cf. Figure 7a), associated with mean temperatures below 18°C. On the contrary, Spain and western France are already affected by southwesterly winds associated with the approaching ridge, leading to higher temperatures ($\geq 21^\circ\text{C}$) there. The mean initial temperature of the tracked air parcels 3d before arriving at the selected location is 5.4°C, and they subsequently undergo a temperature increase of about 10.1°C in 3d (Figure 7f). This increase is partly due to adiabatic warming, corresponding to a mean temperature rise of 5.7°C, which is linked to a mean pressure increase of 62 hPa. It is worth noting that this subsidence is higher between 3d and 1d before arrival and subsequently slows down when the air parcels get close to the surface (Figure 7e). Diabatic heating ~~warming~~, likely ~~resulting to result~~ from surface fluxes, increases the air temperature by 4.4°C ~~in the mean, mainly on average, primarily~~ on the last day before arrival. ~~Therefore, all three processes—advection, adiabatic warming, and diabatic heating—warming—contribute to determining the near-surface temperature at t-1~~ (Figure 7k).

On the day of the events (t), the trough-ridge pattern typically shifts eastward (~~Fig. S6b~~), such that Central Europe also gets under the influence of the southwesterly wind ~~flow~~ ahead of the trough (on the western flank of the ridge) and the near-surface temperature rises above 18°C (Figure 6b). This warming is associated with the arrival of air masses from western continental Europe (Figure 7b). These air parcels have a mean initial temperature of 9.3°C at -3d, which is substantially warmer than the air masses arriving at t-1, with a subsequent temperature increase of 11.4°C in 3d (Figure 7f). This warming is attributed to adiabatic warming (4.5°C in the mean, ~~mean descent of 47~~ with a mean descent of 47 hPa) and strong diabatic heating (6.9°C in the mean). Comparing the ~~contribution of processes between the two days shows that warm advection (3.9°C, Figure 7k) is the predominant factor driving the DTDT increase~~ contributions of processes between the two days reveals that warm air advection (3.9°C, Figure 7k) is the predominant factor driving the increase in DTDT. Further warming

is facilitated by increased diabatic processes (2.5°C in the mean). Adiabatic warming, ~~(-1.2°C),~~ on average, has a small negative contribution ~~((-1.2°C, descent is larger at t-1 compared to t), albeit with the descent is larger at t-1 compared to t),~~
435 ~~albeit with a~~ large ~~variability~~variation between events (Figure 7k).

DJF ~~warm events~~ warming events are dominated by a ridge pattern over western Europe, which weakens on the day of the events, associated with a more zonally oriented flow bringing a larger fraction of warmer maritime air masses to the selected location, which is in contrast to the mainly continental air parcel origin at t-1 (Figs. S73a-b and S84a-b). This change in
440 origin and the associated warm advection and adiabatic warming are the ~~main~~ leading causes of the DTDT increase, whereas diabatic ~~warming-cooling (0 on both days -5.5K on both days)~~ does not differ greatly between the two days (Figs. S8g and k4).



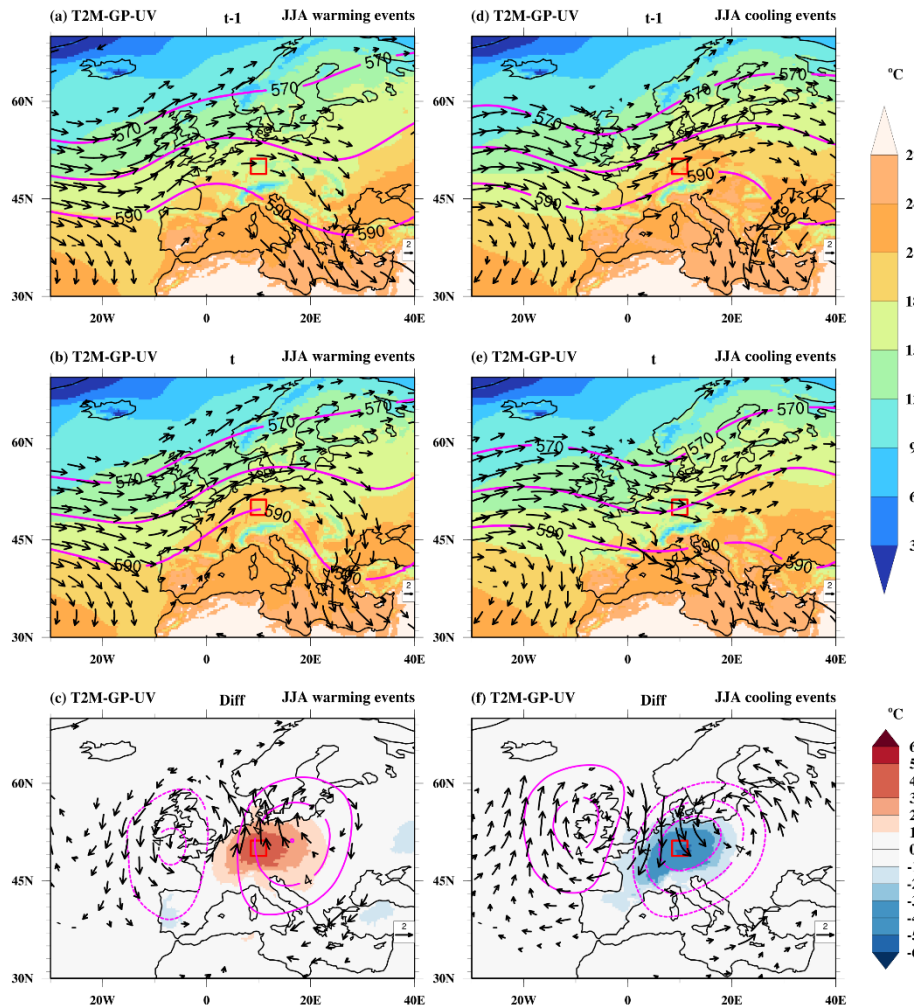


Figure 6. Composite of near-surface temperature (T2M, °C, color shading), wind at 850 hPa (UV, m/s, vectors), and geopotential height at 500 hPa (GP, gpm, magenta contours) on the (a, d) previous day (t-1), (b, e) event day (t) and (c, f) difference (diff) of event day and previous day of the warming (a-c) and cooling (d-f) events during June-August (JJA) at a selected grid point in Europe (red box). Note that (in a-b and d-e) wind vectors ≥ 4 m/s and (in c, f) wind anomalies ≥ 1 m/s are plotted. The dotted and bold magenta contour in c and f indicates negative and positive geopotential height differences, respectively.

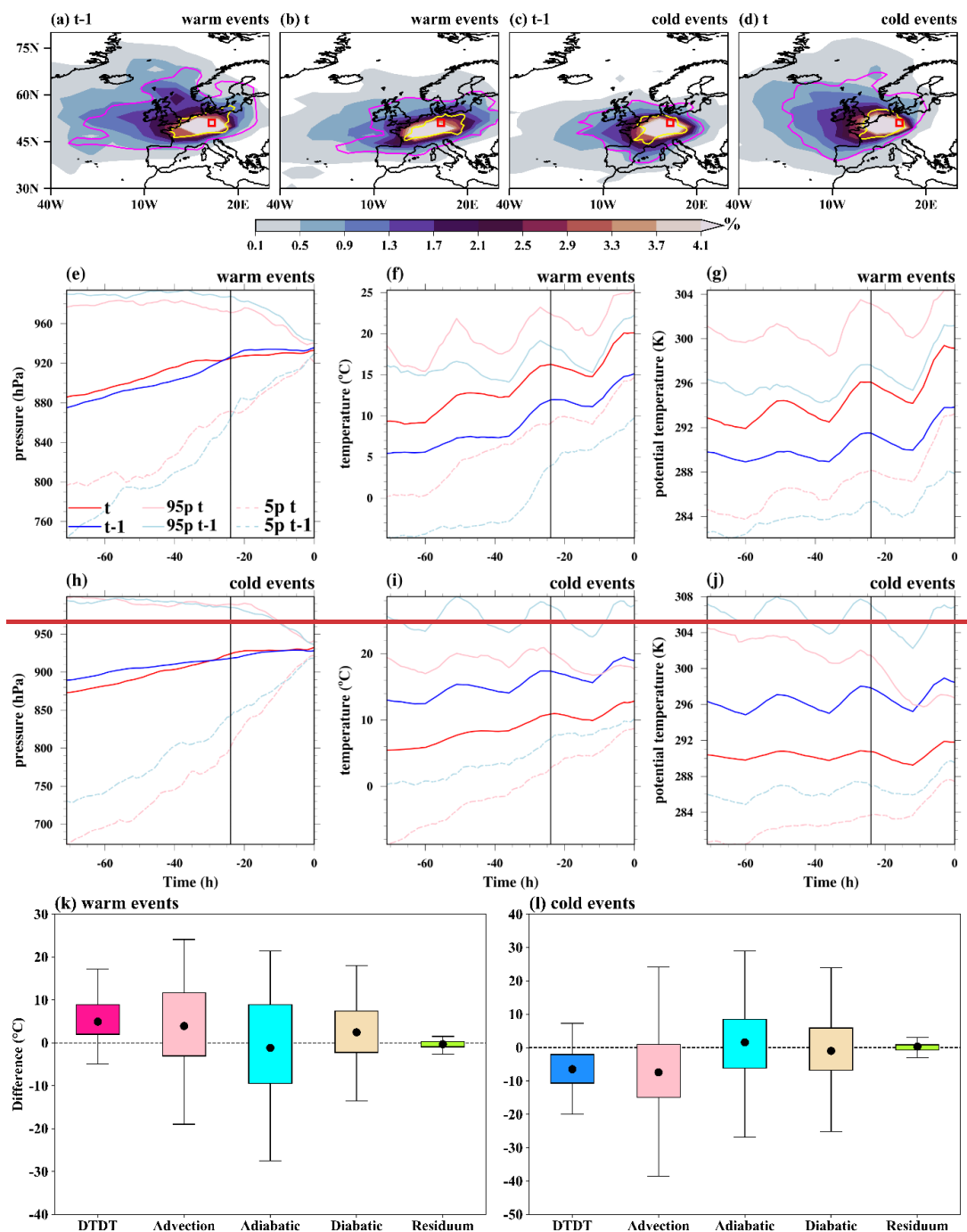
Composite of near-surface temperature (TEM, °C, color shading), wind at 850 hPa (UV, m/s, vectors), and Geopotential height at 500 hPa (GP, gpm, magenta contours) on the (a, c) previous day (t-1) and (b, d) event day (t) of the warm (a,b) and cold events (c,d) during June-August (JJA) at a selected grid point in Europe (red box). Note that wind vectors ≥ 5 m/s are plotted.

During the day preceding JJA ~~cold events-cooling events~~ (t-1), relatively high near-surface temperatures ($\geq 18^\circ\text{C}$) in Central Europe are associated with ~~the southwesterly flow and warm air advection linked to a trough over the British Isles and a ridge downstream over Scandinavia~~ (Figures 6c, 7e) ~~southwesterly winds and warm air masses linked to a trough over the~~

460 British Isles and a ridge downstream over Scandinavia (Figure 6d and 7c, Fig. S6c). The air parcels are already relatively warm 3d before they arrive at the selected location (mean temperature of 13.1°C, Figure 7i) and are further heated by 5.9°C in 3d. Both adiabatic warming during their descent (3.7°C, Figures 7h-i) and diabatic heating (2.2°C, Figure 7j) contribute to this temperature increase.

465 On the day of the events (t), Central European temperature decreases substantially to values below 18°C, linked to a weakening of the upstream trough and eastward propagation of the ridge, leading to more zonal flow conditions (Figure 6e and Fig. S6de). Northwesternly winds carry cold, maritime ~~airmasses toward the target location, with an initial temperature of 5.4°C (Figure 7d and Figure~~ air masses toward the target location, with an initial temperature of 5.4°C (Figures 7d and 7i). These air parcels are further warmed by 7.3°C due to strong adiabatic warming ~~-(5.7°C, -(5.7°C, corresponding to a mean~~
470 descent of 60 hPa, Figure 7h) and some diabatic heatingwarming (1.6°C, Figure 7j) in 3d. Comparing the process contributions on the two days ~~shows that DTDT cold events occur predominantly due to a shift from warm to cold air advection (mean temperature change of -7.7°C, reveals that DTDT cooling events occur predominantly due to cold air advection by northerly winds (Figure 6f), with a mean temperature change of -7.7°C (Figure 7l)~~. This advective effect is partly balanced by an increase in adiabatic warming (2°C). The reduced diabatic heatingwarming is small but possesses
475 substantial ~~events to events~~event-to-event variabilityvariation (Figure 7l).

DJF ~~cold events~~cooling events are triggered by a shift from westerly to northerly winds ahead of a developing ridge over the eastern North Atlantic (Figs. ~~S3e-d and Figs. S4e-d~~S7e-f and S8c-d). Air masses arriving ~~at~~on the day of the events ~~(t)~~ have a much lower temperature at their origin (-3d) compared to the preceding dayt-1 due to this northward shift in the source
480 location (Figs. S84c-d) and a typically higher altitude (Fig. S84h-j). This leads to a pronounced contribution of advection to the DTDT decrease, which is, however, partly compensated by increased subsidence and adiabatic warming on the day of the events and a slight increase in diabatic heating (Figs. S84h,i,j,l).



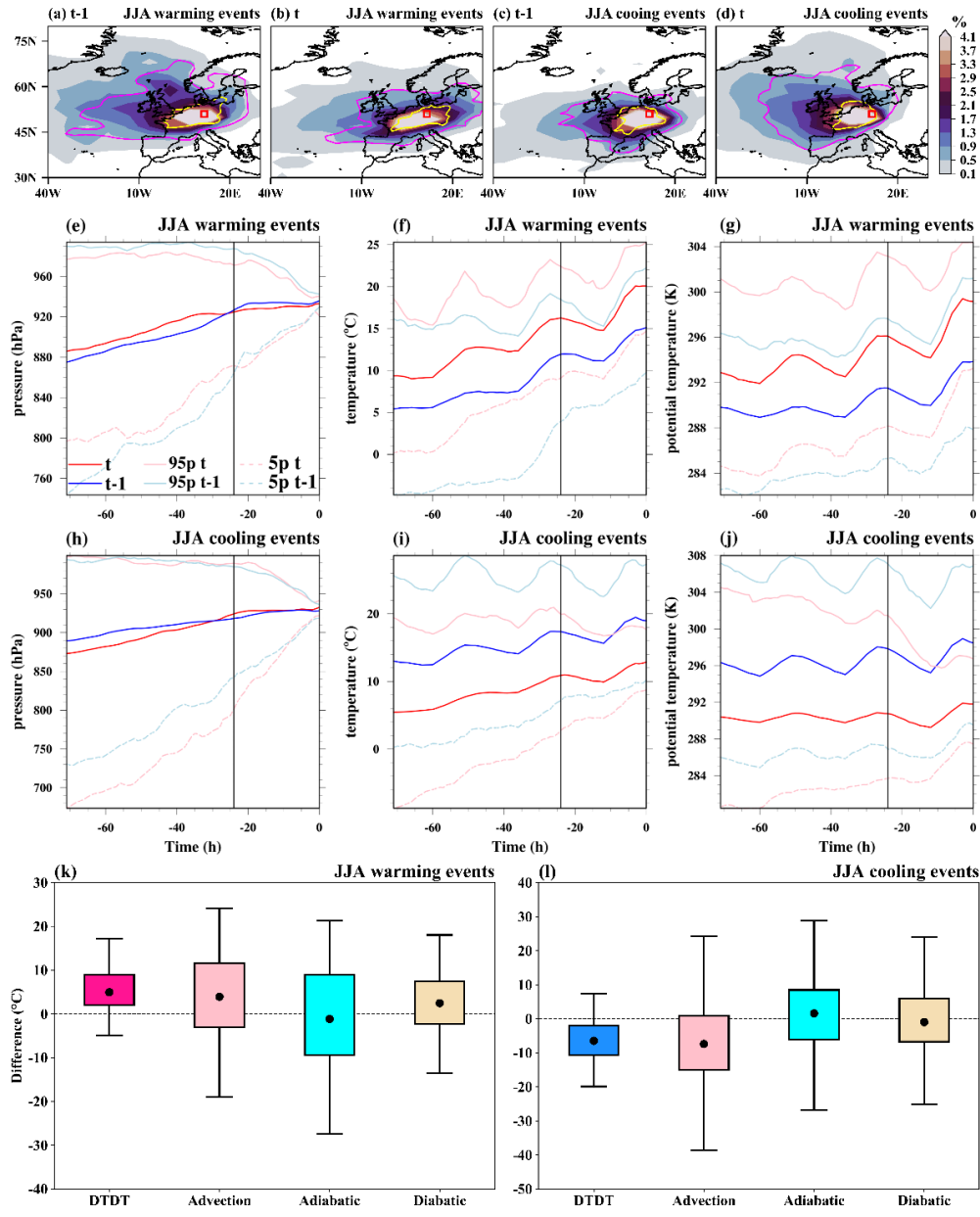


Figure 7. The spatial distribution of trajectories initiated on the previous day (t-1) and event day (t) for both June-August (JJA) warming and cold events-cooling events over Europe. In the top row, the color-shading illustrates the air parcel trajectory density (%) based on the position between -5d-5d and 0d. The magenta and yellow contours represent 0.5% particle density fields at -3d and -1d-3d and -1d, respectively. The red box shows the selected grid point-point over Europe. The Lagrangian evolution of distinct physical parameters (pressure, temperature, potential temperature) along the air parcel trajectories for both warming (2nd row) and cold events-cooling events (3rd row) is presented in panels e-j. Panels k and l show the contribution of the different physical processes to the genesis of DTD extremes extreme DTD changes according to Eq. (6), which refers to a 3d-time scale. The residuum is attributable to numerical inaccuracies in the computation of derivatives in Eq. (6). The box spans the 25th

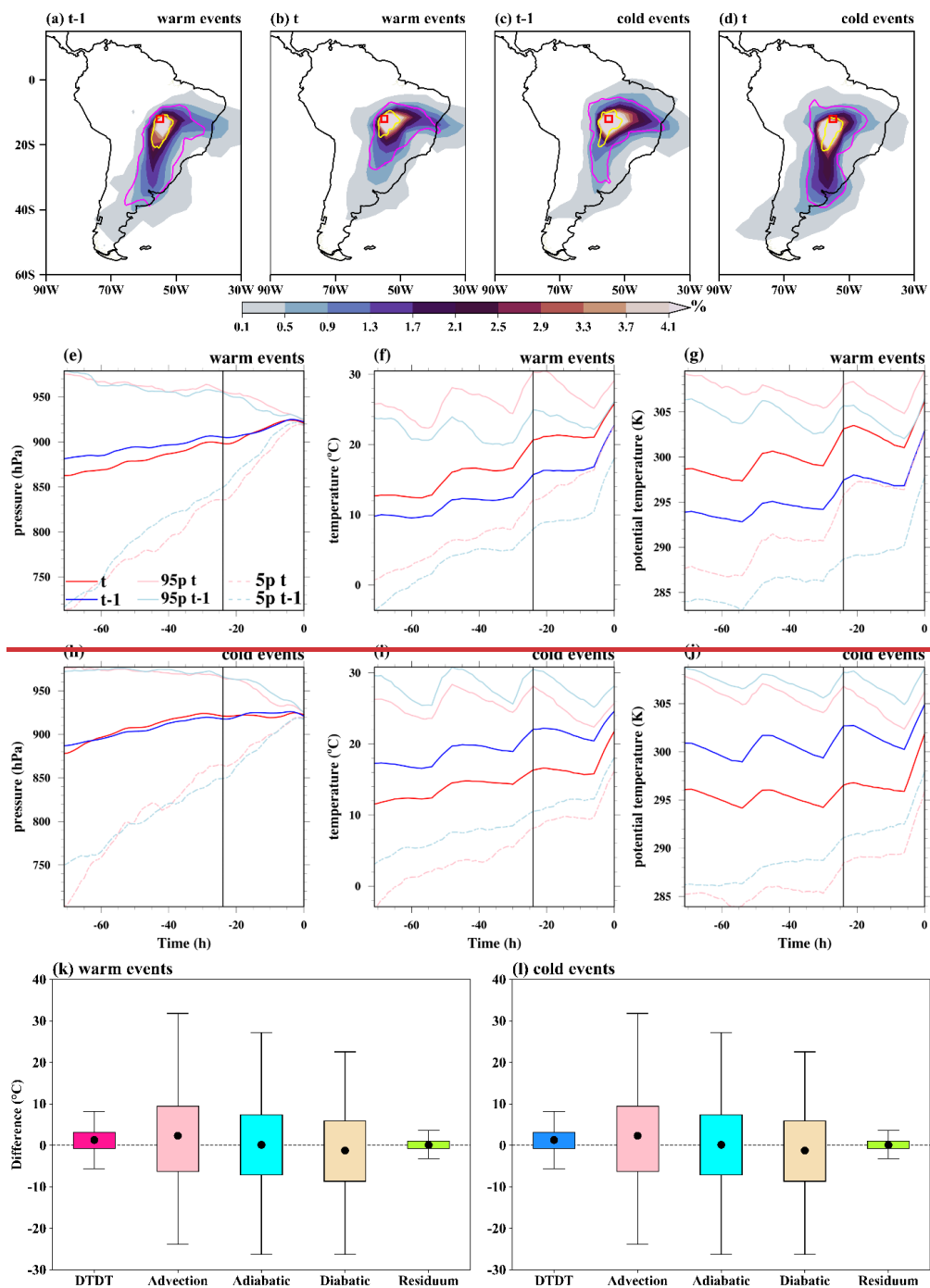
and 75th ~~percentile-percentiles~~ of the data; the black dot inside the box gives the mean of the related quantities, and 1.5 times the interquartile range gives the whiskers.

495 3.2.3 Tropics: South America

To ~~systematically~~ investigate the mechanism of extreme DTDT changes in the deep tropics during DJF and JJA, we select a specific location in South America (~~56°W and 13°S~~) and also compare results with South Africa (~~24°E and 13°S~~, Figs. ~~S6 and SS10-117~~), where physical processes appear to be similar.

500 During JJA, ~~DTDT extremes~~extreme DTDT changes over tropical South America are associated with distinct patterns~~the~~, particularly in the wind field (Figs. ~~S95a-fd~~). ~~At~~On the day preceding the warming events (t-1), the selected location lies in the region of a strong horizontal temperature gradient, with higher temperatures ($\geq 22^{\circ}\text{C}$) ~~northeast and lower temperatures~~ ($\leq 20^{\circ}\text{C}$) ~~southwest of it~~to the northeast and lower temperatures ($\leq 20^{\circ}\text{C}$) to the southwest. The latter may be associated with extratropical influences, mainly through a trough over Argentina and the South Atlantic (Fig. ~~S95a~~). Air parcels arriving on
505 this day originate (at -3d) mainly from the south (Figure 8a), with a mean initial air temperature of 9.7°C that gradually increases due to adiabatic warming (4°C , descent of 41 hPa) and strong diabatic ~~heating~~warming (9.9°C , Figures 8e-g).

On the ~~day of the events (t), the trough weakens, and~~ day of the warming events (t), the trough weakens, and the winds turn easterly, which is associated with a larger fraction of air parcels originating from the east (Fig. ~~S95b~~ and Figure 8b). These
510 air parcels are initially warmer (12.7°C on average) than at t-1 (Figure 8f and Fig. S9c) and again experience an average temperature increase (by 13.9°C), influenced by adiabatic warming (5.6°C , 58_hPa descent) and strong diabatic ~~heating~~warming (8.3°C , Figures 8e-f). When examining the physical processes across consecutive days, the DTDT ~~warm events~~warming events can be attributed to a combination of factors, including warm air advection, enhanced adiabatic ~~warming~~heating, and reduced diabatic heating (Figure 8k). ~~Initially, the warm advected air masses experience heating during their descent; this temperature increase is mitigated by a less pronounced diabatic heating~~warming on the events event's day (Figures 8e-g). ~~Therefore, the primary contribution to warming comes from advection and some additional adiabatic warming.~~Notably, all three physical factors possess substantial event-to-event variation (Figure 8l).



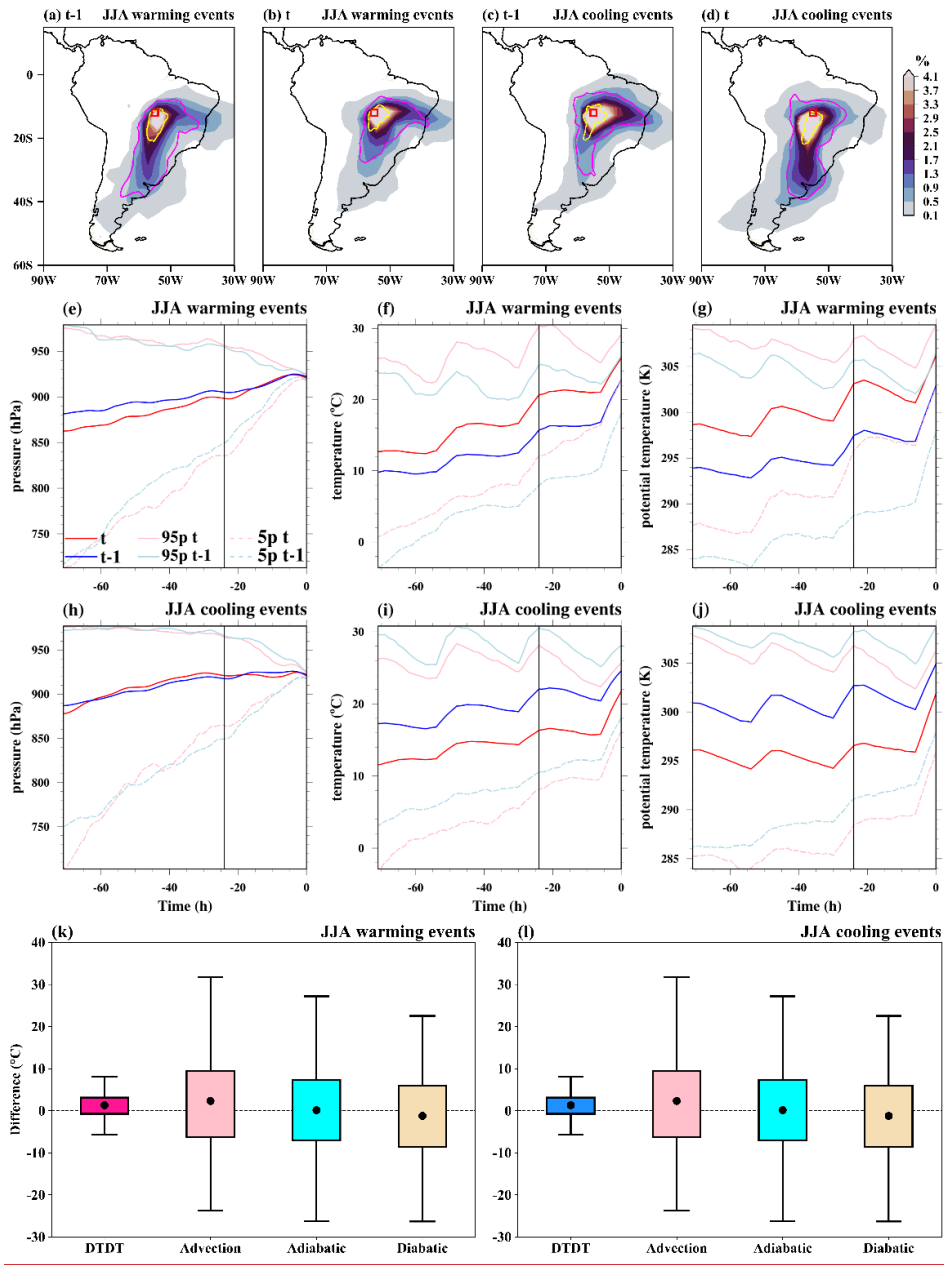
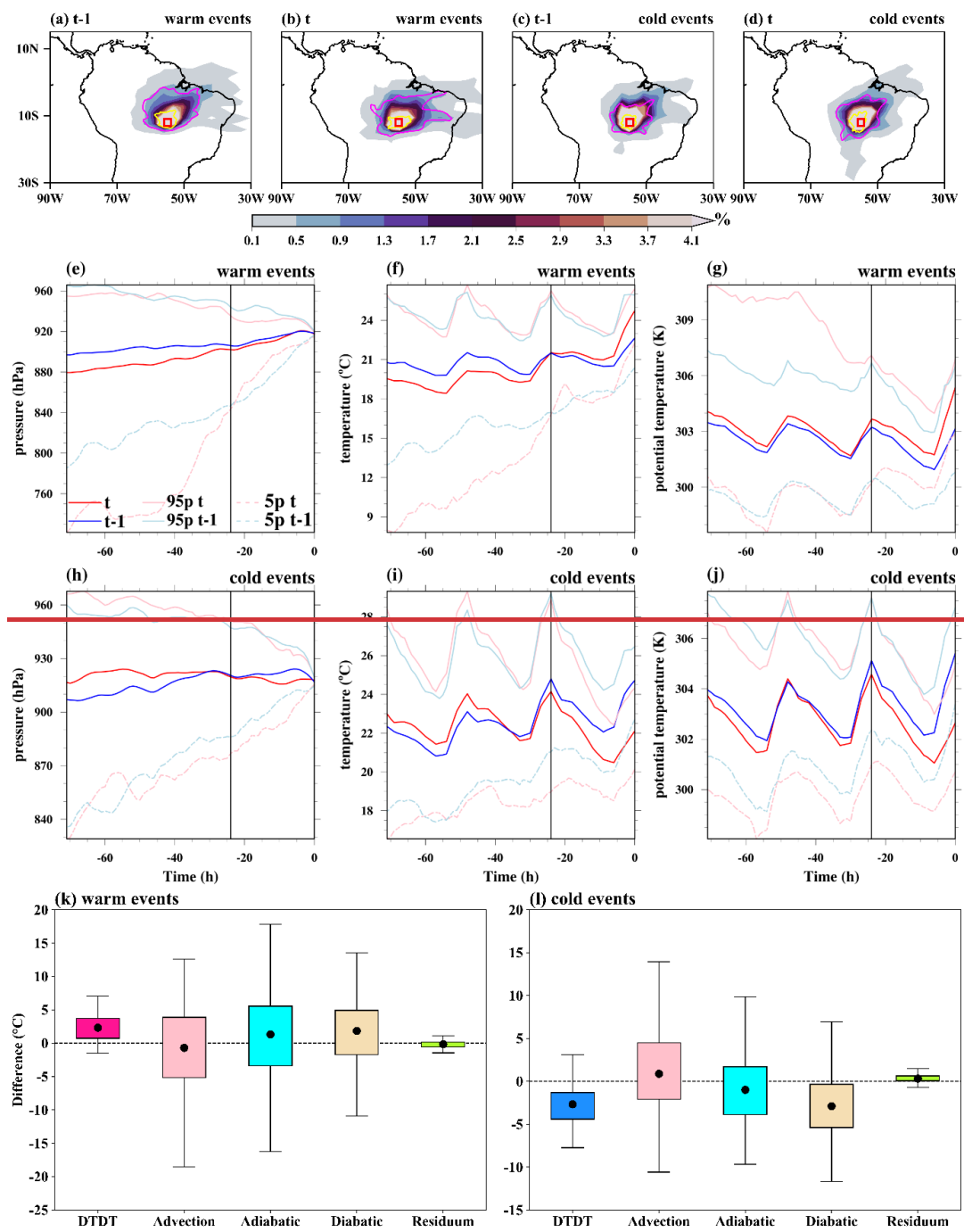


Figure 8. The spatial distribution of trajectories initiated on the previous day (t-1) and event day (t) for both June-August (JJA) warming and cold events-cooling events over South America. In the top row, the color-shading illustrates the air parcel trajectory density (%) based on the position between -5d-5d and 0d. The magenta and yellow contours represent 0.5% particle density fields at -3d and -1d, respectively. The red box shows the selected grid point over South America. The Lagrangian evolution of distinct physical parameters (pressure, temperature, potential temperature) along the air parcel trajectories for both warming (2nd row) and cold events-cooling events (3rd row) is presented in panels e-j. Panels k and l show the contribution of the different physical processes to the genesis of DTDT extremes according to Eq. (6), which refers to a 3d-time scale. The residue is attributable to numerical inaccuracies in the computation of derivatives in Eq. (6). The box spans the

25th and 75th ~~percentile percentiles~~ of the data; the black dot inside the box gives the mean of the related quantities, and 1.5 times the interquartile range gives the whiskers.

In contrast to JJA, ~~DTDT extremes~~extreme DTDT changes in DJF are not associated with ~~specific clear~~ circulation patterns. The origins of air parcels at -3d are clustered around the selected location, indicating that primarily local effects lead to the DTDT changes (Figures 9a-d). ~~Additionally, the advected temperature of air parcels on t and t-1 converge at -24h, negatively contributing to the local DTDT change and indicating that adiabatic warming is not responsible for this change~~(Figure 9f), and ~~there~~there are only minor changes in descent and adiabatic warming between t and t-1 (Figure 9e,k). ~~Negative contributions of advection and increased adiabatic warming~~The cancel each other, such that DTDT changes are predominantly due to differences in diabatic heating on the last day before the air parcels arrive at the selected location (Figures 9e-l). To better understand these local, diabatic effects, we analyse composites of cloud cover and precipitation based on ERA5 data (Figure 10a). For DTDT warming events, high cloud coverage (90-95%), along with substantial cumulative precipitation (~~108-140~~ mm/day), is observed at t-1 across the study region, resulting in reduced diabatic heating and colder temperatures (Figures 9f, ~~g~~ and 10a). In contrast, cloud cover (70-75%) and precipitation (~~2-64~~ mm/day) decrease on the day of the events, presumably contributing to larger diabatic heating and higher temperatures (Figures 9f, g, k, and 10b). Thus, the DTDT change during ~~warm events~~warming events is linked to a transition from primarily cloudy and wet to less cloudy and drier conditions (Figure 10c). This indicates an essential role of albedo changes and solar radiative heating in triggering the temperature increase.

The day before JJA ~~cold events~~cooling events (t-1) is characterized by high near-surface temperatures ($\geq 24^{\circ}\text{C}$) at the selected location and a temperature gradient to the south (Fig. ~~S95d~~e). Easterly winds prevail over the study area, bringing in initially warm air parcels (17.3°C mean temperature at -3d) that undergo an additional temperature rise (7.7°C) due to adiabatic warming (3.3°C) and diabatic heating (4.4°C). In contrast, on the day of the events, colder air masses are transported to the selected location by southerly winds upstream and equatorward of a subtropical trough over south-east South America and the South Atlantic (Figure 8d and Fig. ~~S95e~~d), again pointing to a potential role of extratropical-tropical interactions (Fig. S9f). The air parcels originally haved lower temperatures (11.4°C) than at t-1. They undergo a temperature increase (10.8°C) due to adiabatic warming (4.4°C) and diabatic heating (6.4°C , Figures 8h-j). Comparing the two days indicates that JJA ~~cold events~~cooling events are driven by cold air advection, which is partly counterbalanced by increased adiabatic warming and diabatic heating, with larger event-to-event variabilitywarming (Figure 8l).



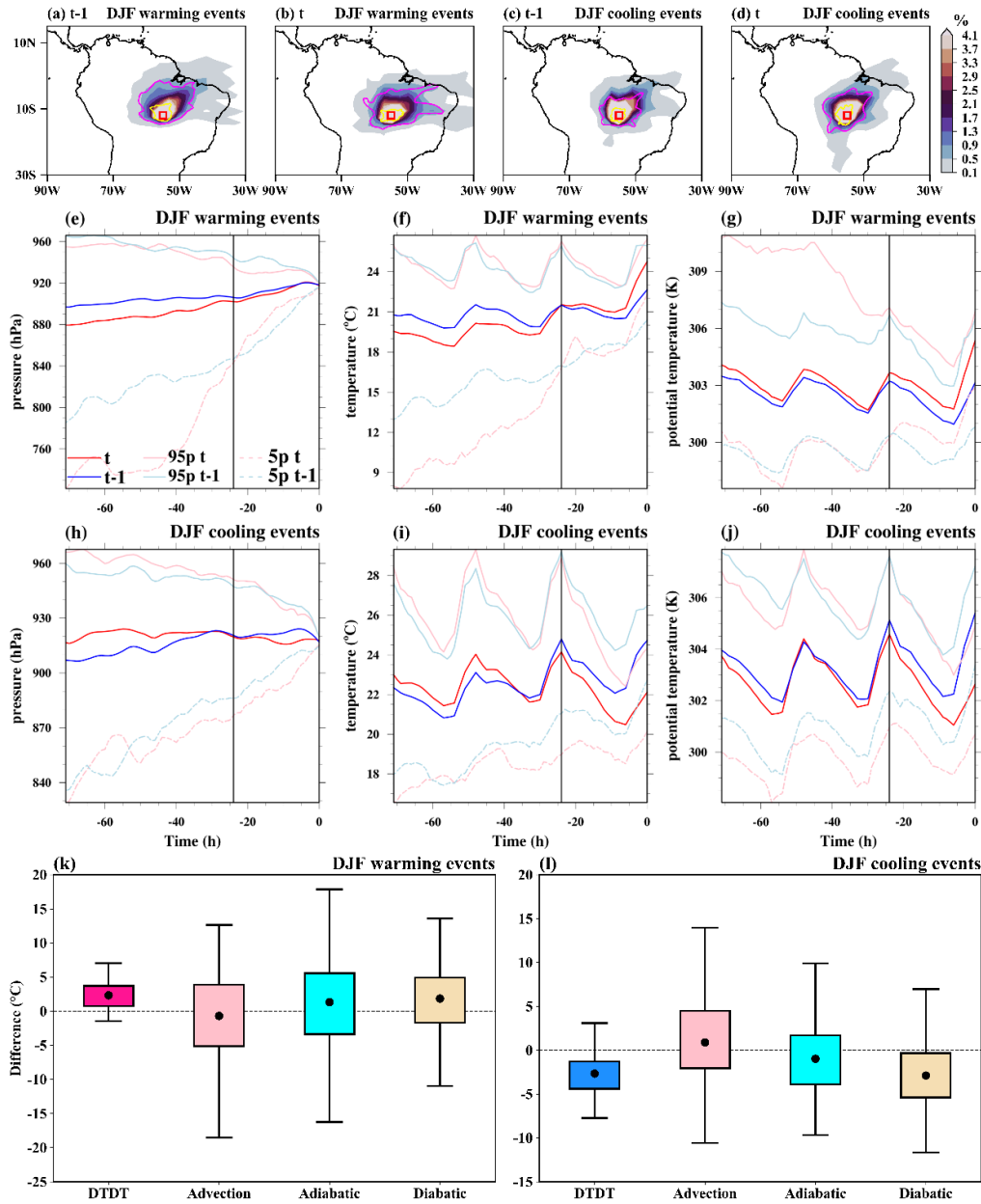
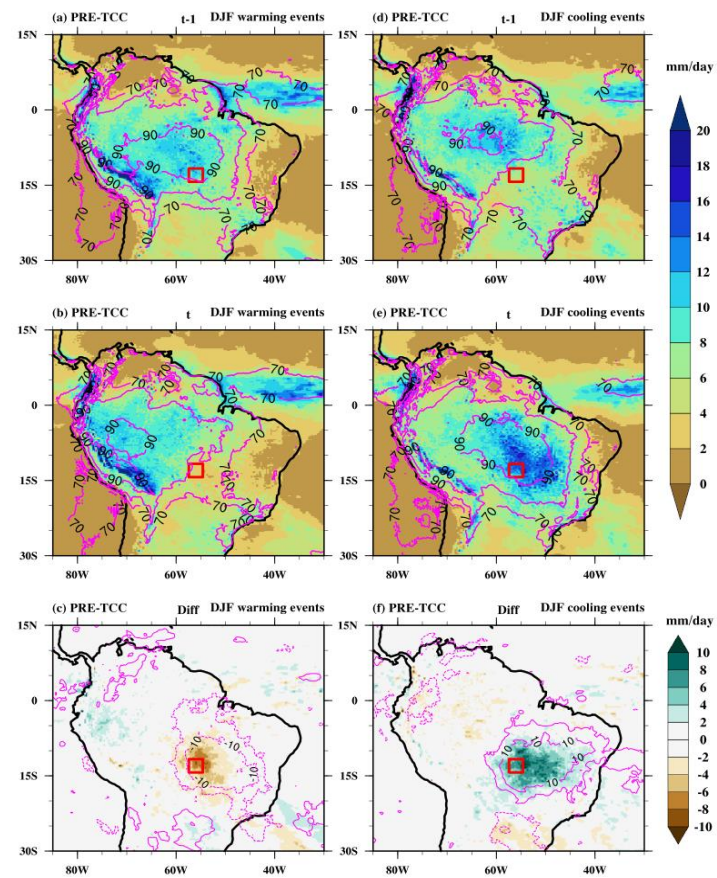


Figure 9. The spatial distribution of trajectories initiated on the previous day (t-1) and event day (t) for both December-February (DJF) warming and cold events-cooling events over South America. In the top row, the color-shading illustrates the air parcel trajectory density (%) based on the position between -5d-5d and 0d. The magenta and yellow contours represent 0.5% particle density fields at -3d and -1d, respectively. The red box shows the selected grid point over South America. The Lagrangian evolution of distinct physical parameters (pressure, temperature, potential temperature) along the air parcel trajectories for both warming (2nd row) and cold events-cooling events (3rd row) is presented in panels e-j. Panels k and l show the contribution of the different physical processes to the genesis of DTDT extremes according to Eq. (6), which refers to a 3d-time scale. The residuum is attributable to numerical inaccuracies in the computation of derivatives in Eq. (6).

The box spans the 25th and 75th ~~percentile-percentiles~~ of the data; the black dot inside the box gives the mean of the related quantities, and 1.5 times the interquartile range gives the whiskers.

570

Similar to the DJF warm~~ing~~-events, the DTDT change during DJF ~~cold-events-cooling events~~ is primarily driven by reduced diabatic heating on the last day before the air parcels arrive at the target location (Figures 9h-j), which can be attributed to variations in local conditions (~~Figures 10e-d~~). Again, like warm~~ing~~ events, Figures 10~~de-fd~~ indicate that these variations are associated with changes in cloud cover and precipitation: on the preceding~~At t-1 day~~, relatively lower cloud cover (70% ~~-to~~ 80%) is observed, coupled with lower total precipitation (~~24-to~~ 8 mm/day) across the study area, ultimately resulting in higher temperatures (Figure 10~~de~~ and Figure 9i). In contrast, on the day of the events, cloud cover (90-95%) and precipitation (1~~24~~-20 mm/day) are higher, contributing to colder temperatures (Figure 10~~ed~~ and Figure 9i). Thus, DJF ~~DTDT cold-events-cooling events~~ are linked to a transition from less cloudy and drier to cloud-covered and wet conditions (Figure 10f), again indicating a significant role of solar radiative heating (reduced diabatic heating, see Figure 9l).



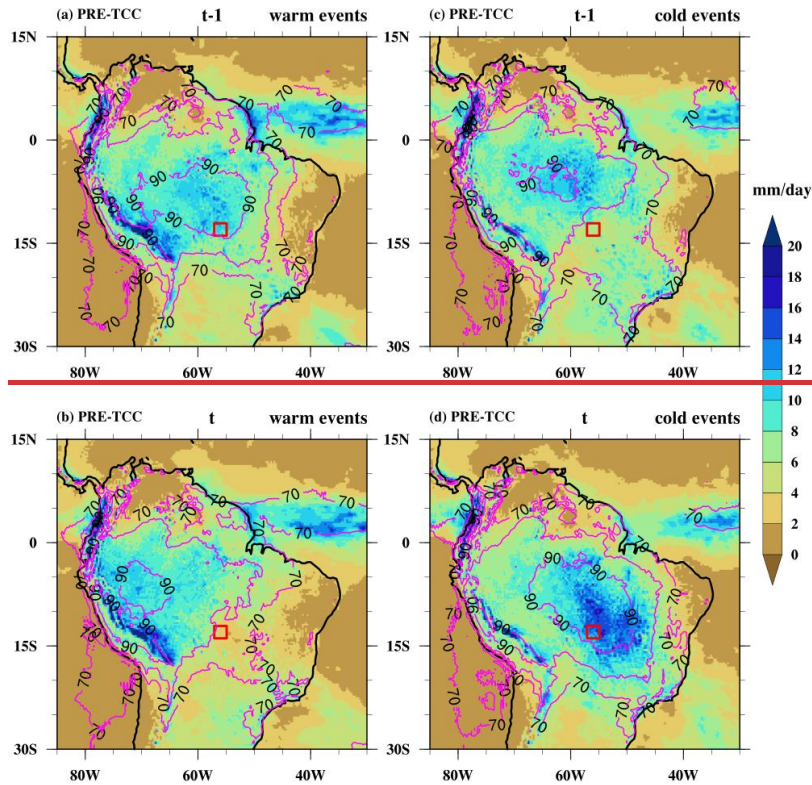


Figure 10. Composites of precipitation (PRE, mm/day, colour shading) and total cloud cover (TCC, %, magenta contours) on the (a, d) previous day (t-1) and (b, e) event day and (c, f) (+t) difference (diff) of event day and previous day of the warming (a-c) and cooling (d-f) events during December-February (DJF) at a selected grid point in South America (red box). The dotted and bold magenta contour in c and f indicates negative and positive total cloud cover differences, respectively.

of warm events (a,b) and cold events (c,d) during December-February (DJF) at a selected grid point in South America (red box).

3.2.4 Southern Hemisphere Subtropics: Australia

To systematically investigate the mechanism driving DTDT extremes over the subtropics in the southern hemisphere during DJF and JJA, we select a specific location in Australia. We select a specific location in southern Australia to investigate the mechanism driving extreme DTDT changes over the subtropics in the southern hemisphere during DJF and JJA (140°E and 37°S).

On the day preceding DJF warm events-warming events (t-1), the selected location lies in a region of weak winds in the center of a ridge and within a strong meridional temperature gradient (Fig. S12a), with higher temperatures over the continent to the north ($\geq 24^{\circ}\text{C}$) and lower temperatures over the Southern Ocean ($\leq 16^{\circ}\text{C}$, Figure 11a). The tracked air parcels, at 3d-3d, are mostly located near the selected point or to its southwest (Figure 12a). Starting with relatively low

temperatures (1.8°C on average), they undergo substantial subsidence (147 hPa) and adiabatic warming, resulting in a noteworthy temperature increase of 13.8°C (Figures 12e-f). In addition, they experience weak diabatic heating on the day before arrival (1.8°C, Figure 12g).

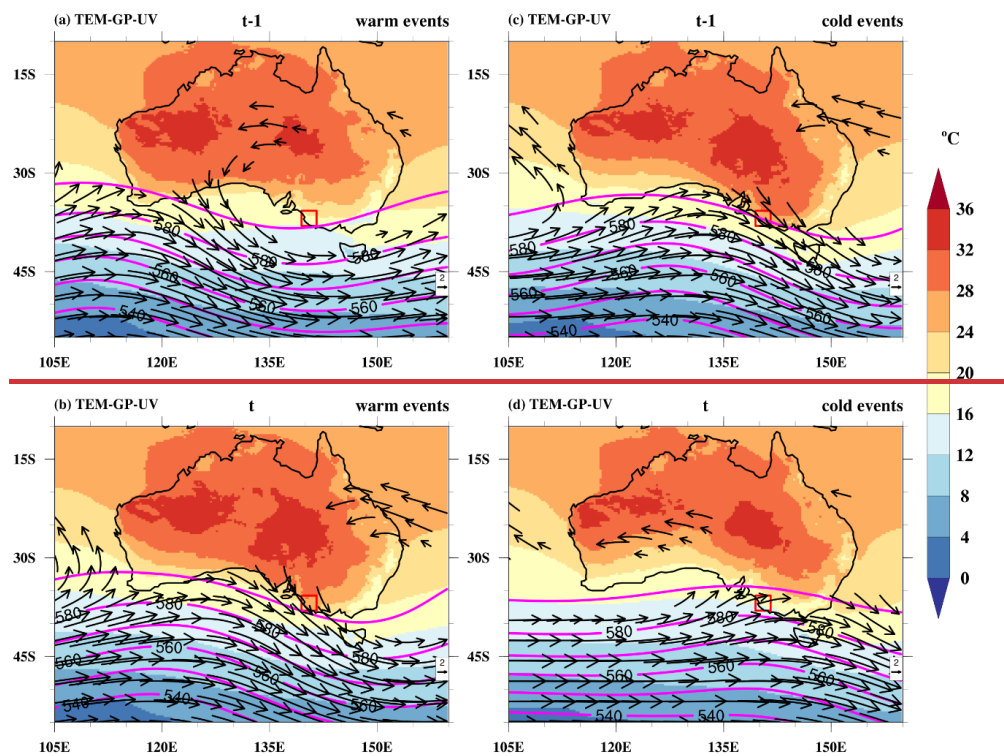
600

The temperature increase on the day of the ~~events is associated with an event is associated with~~ intensification and eastward shift of a trough towards the Great Australian Bight and ~~the result froming associated~~ northerly ~~winds (Fig. S12b)~~ airflow, bringing warm, continental air mass to the selected location (Figures 11**~~b and~~** 12b). These air parcels are slightly warmer (5.1°C) at -3d compared to t-1, also experience adiabatic warming during their ~~vertical~~ descent (9.4°C, mean descent of 98 hPa), but are much more strongly affected by diabatic heating (9.9°C, Figures 12e-g). DJF ~~warm events-warming events~~ over the southern coast of Australia thus ~~results-result~~ from a shift from oceanic to continental air masses (Figure 11c and Fig. S12b), resulting in amplified warm air advection (3.3°C) and, more importantly, increased diabatic heating (8.1°C), most likely due to surface fluxes over the warm continent, while reduced descent and adiabatic warming (-4.4°C) have a dampening effect, with substantial variability between events (Figure 12l).

610

The atmospheric circulation (not shown) and backward air parcel distribution during JJA ~~warm events-warming events~~ resemble those of DJF (Fig. S13a-b) ~~(Figs. S8a-b)~~. However, most probably related to the weaker surface fluxes in Austral winter, diabatic heating does not contribute substantially to the temperature evolution along the trajectories (Fig. S13g). Consequently, the ~~warm events-warming events~~ are primarily due to warm air advection (5.9°C), with both the adiabatic warming (-2.2°C) and diabatic (-2.2°C) and diabatic heating (-1.4°C) terms having a ~~smaller~~ damping effect (Fig. S13k).

615



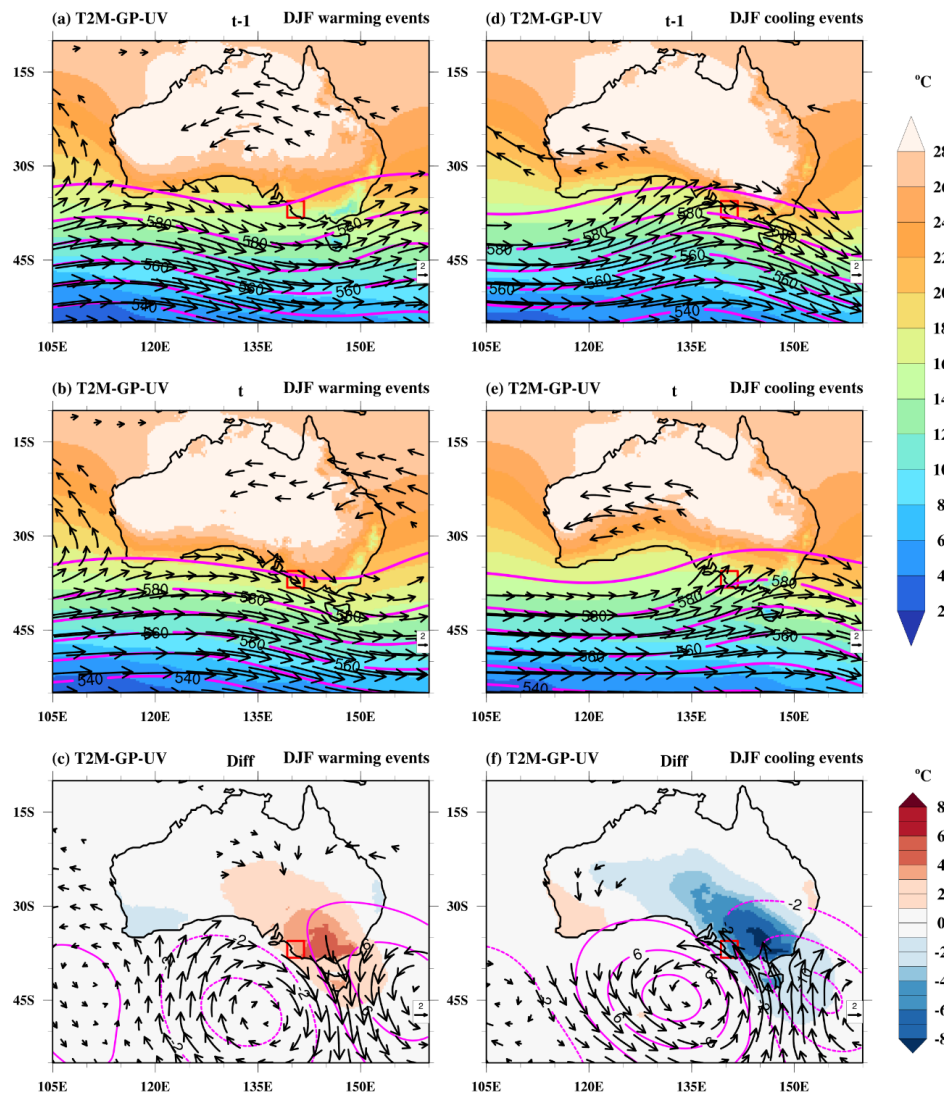
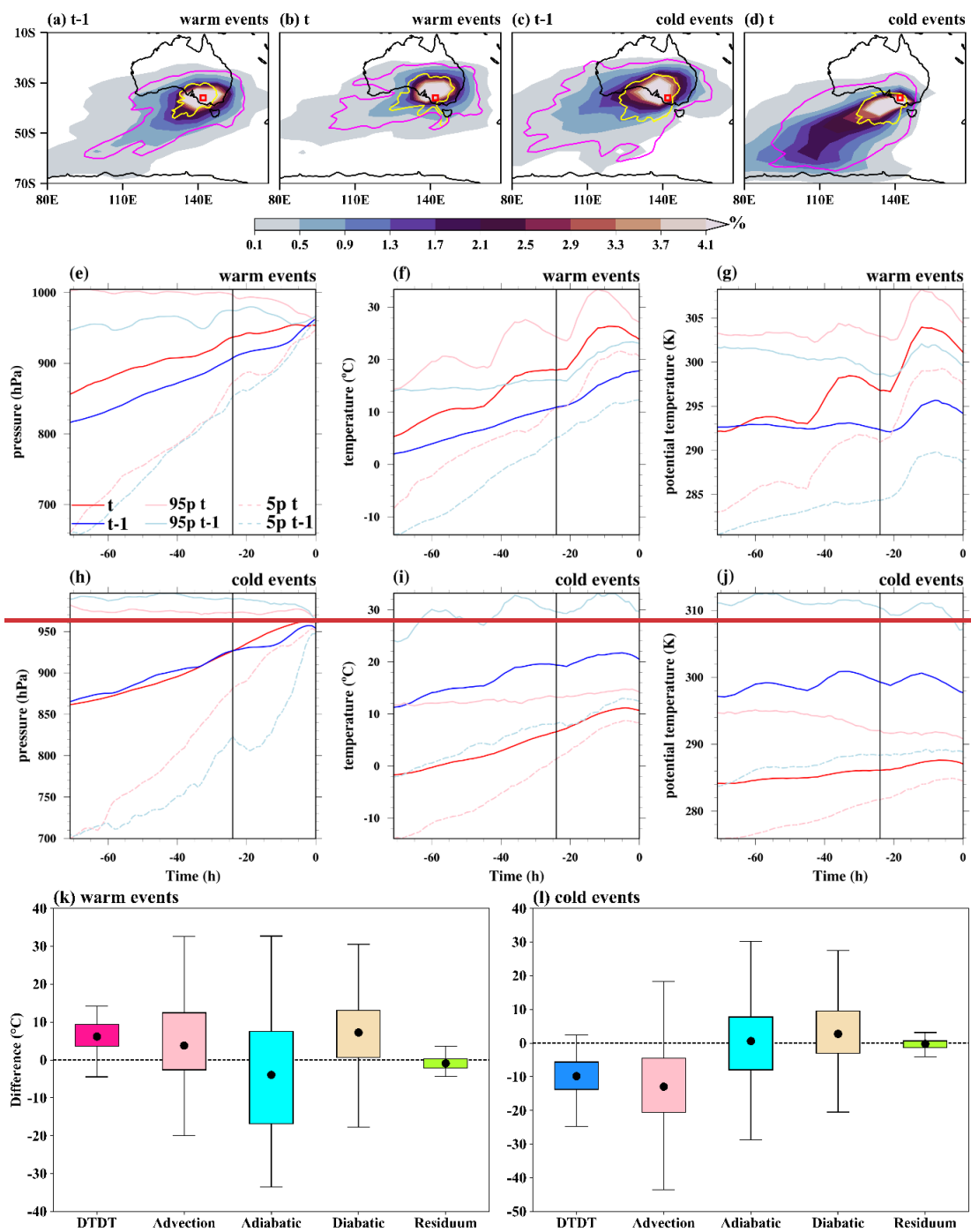


Figure 11. Composite of near-surface temperature (T2M, °C, color shading), wind at 850 hPa (UV, m/s, vectors), and geopotential height at 500 hPa (GP, gpm, magenta contours) on the (a, d) previous day (t-1), (b, e) event day (t) and (c, f) difference (diff) of event day and previous day of the warming (a-c) and cooling (d-f) events during December-February (DJF) at a selected grid point in Australia (red box). Note that (in a-b and d-e) wind vectors $\geq 4\text{m/s}$ and (in c, f) wind anomalies $\geq 1\text{m/s}$ are plotted. The dotted and bold magenta contour in c and f indicates negative and positive geopotential height differences, respectively.

Composite of near-surface temperature (TEM, °C, color shading), wind at 850 hPa (UV, m/s, vectors), and Geopotential height at 500 hPa (GP, gpm, magenta contours) on the (a, e) previous day (t-1) and (b, d) event day (t) of warm (a,b) and cold events (c,d) during December-February (DJF) at a selected grid point in Australia (red box). Note that wind vectors $\geq 5\text{m/s}$ are plotted.

On the day preceding DJF ~~cold events~~ cooling events (t-1), a trough is located west of the selected grid point, associated with the advection of warm, continental air masses (Figures 11d, ~~e and~~ 12c, and Fig. S12c). The air particles originate at a relatively high temperature (11.2°C) and undergo subsequent adiabatic warming (8.5°C, mean descent of 89 hPa), while diabatic heating is small (Figures 12h-j). ~~Whereas~~ On the day of the events, the trough has moved eastward, such that the selected location gets under the influence of southwesterly windflow on its western side (Figure 11~~e-d~~ f and Fig. S12d), leading to the advection of colder, oceanic air masses with a mean temperature of -1.8°C at -3d (Figures 12d-e). This shift to cold air advection (-13°C) is the main reason for the DTDT ~~cold events~~ cooling events (Figure 12l). Adiabatic warming is very similar between the two days, while diabatic heating (2.8°C) increases slightly, dampening the temperature decrease.

Similar to DJF, JJA ~~cold events~~ cooling events are characterized by a shift from continental to maritime air masses (Figs. S13~~8~~ c-d). The events are mainly triggered by cold air advection (-10.8°C), mitigated by increased diabatic heating (6.6°C), with adiabatic heating (1.3°C) changes being of minor importance (Fig. S13~~h-i~~ and 8l).



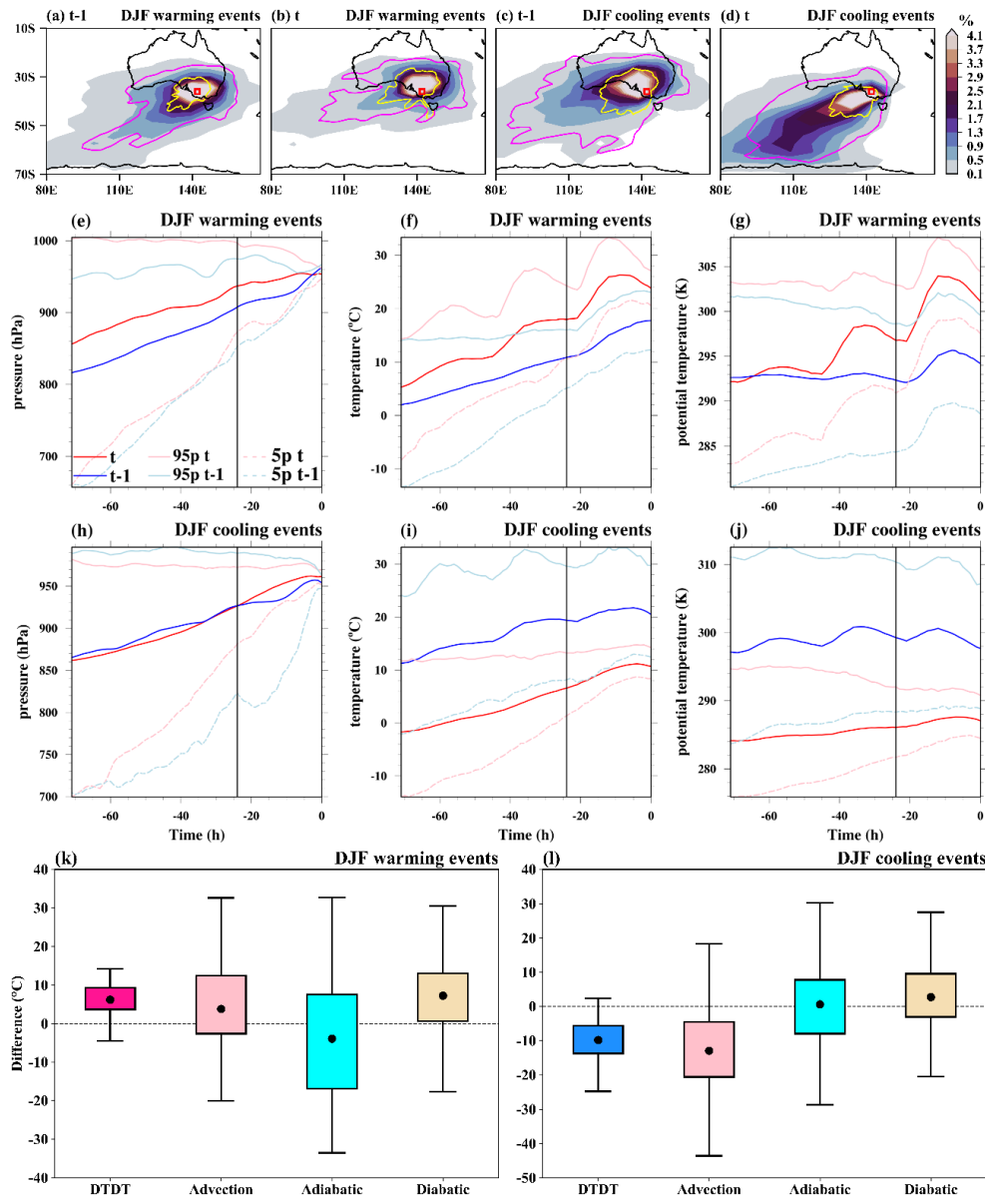


Figure 12. The spatial distribution of trajectories initiated on the previous day ($t-1$) and event day (t) for both December-February (DJF) warming and cold events-cooling events over Australia. In the top row, the color-shading illustrates the air parcel trajectory density (%) based on the position between $-5d$ and $0d$. The magenta and yellow contours represent 0.5% particle density fields at $-3d$ and $-1d$, respectively. The red box shows the selected grid-point over Australia. The Lagrangian evolution of distinct physical parameters (pressure, temperature, potential temperature) along the air parcel trajectories for both warming (2nd row) and cold events-cooling events (3rd row) is presented in panels e-j. Panels k and l show the contribution of the different physical processes to the genesis of DTDT extremes according to Eq. (6), which refers to a 3d-time scale. The residuum is attributable to numerical inaccuracies in the computation of derivatives in Eq. (6). The box spans the 25th and 75th percentile-percentiles of the data; the black dot inside the box gives the mean of the related quantities, and 1.5 times the interquartile range gives the whiskers.

4. Discussion and summary

655 In this study, we have investigated (extreme) DTDT changes and the underlying physical processes. DTDT changes and extremes have a larger magnitude in the extratropics compared to tropical regions during both DJF and JJA, consistent with previous studies (Xu et al., 2020; Zhou et al., 2020). These spatial patterns are associated mainly with differences in the standard deviation of daily temperature, but differences in the temporal autocorrelation also play a role ~~for-in~~ some regional variations. The patterns are generally comparable between ERA5 reanalysis data and ~~HadGHCND_~~ ~~o~~ observations (660 ~~(particularly~~ mainly BEST), with typically larger magnitudes of DTDT changes in ERA5 ~~(mostly compared to HadGHCND)~~ due to both higher standard deviations and lower autocorrelation. The temperatures on the two days associated with extreme DTDT changes are not necessarily extreme by themselves, but themselves but tend to cluster in the tails of the daily temperature distribution.

665 The mechanisms driving extreme DTDT changes (~~cold-events-cooling events~~ below the 5th percentile and ~~warm-events~~ warming events above the 95th percentile) have been analyzed in detail for selected locations, using a combination of Eulerian composites, ~~and Lagrangian process analysis to decompose the effects of advection, adiabatic and diabatic heating on a 3d-time~~ and Lagrangian process analysis to decompose the effects of advection, adiabatic, and diabatic heating/cooling on a 3d-time scale. In the extratropics, extreme DTDT changes are typically associated with distinct synoptic circulation patterns, in particular troughs and ridges in the 500-hPa geopotential height field, similar to extremes of near-surface temperature (White et al., 2023; Parker et al., 2013; Nygård et al., 2023; ~~see also Fig. S7 for a comparison~~). These patterns may be related to specific large-scale modes, such as the North Atlantic Oscillation, ~~Artie~~ Arctic Oscillation, or Southern Annular Mode, which significantly impact air mass advection (Lee et al., 2020; Liu et al., 2023; Dai and Deng, 2021). ~~Such potential linkages can be studied in more detail in future research.~~ Such circulation types and frontal passages influence the distribution of DTDT extremes, showing asymmetry over Europe. In addition, they are likely associated with frontal passages, as explicitly shown for Europe by ~~(Piskala and Huth, (2020). Future research may~~ (Piskala and Huth, (2020). Future research may ~~also study such potential linkages in more detail, also at~~ also study such potential linkages in more detail, also at other locations. (675

Our trajectory analysis shows that changes in advection are the main driver of extreme DTDT changes in the extratropics, while the contributions of adiabatic and diabatic processes are generally smaller and vary more in space and also between warming and cooling events. Changes in descent and adiabatic warming between the two days of an extreme DTDT change are either small or dampen the intensity of the events, for instance, for warming and ~~cold-events-cooling events~~ in Europe and South Asia (Figs. S150c-d) in JJA and ~~in~~ eastern and western North America and south Asia in DJF (Figs. S52a-b and S150a-b), with the exception of ~~warm-events-warming events~~ in eastern North America, and high-latitude North Asia (Figs. S149c-d) in JJA and Europe in DJF, where they contribute positively. Diabatic ~~heating-processes have~~ has a particularly strong effect on extreme DTDT changes in southern Australia, where ~~it~~ they dampens the events' intensity in JJA (685

but strongly amplifies ~~warm events~~ warming events in ~~the the~~ Austral summer. The latter is reminiscent of diabatic effects on wildfires and heatwaves in this region (Quinting and Reeder, 2017; Magaritz-Ronen and Raveh-Rubin, 2023). Apart from this, diabatic processes ~~slightly~~ amplify both warm and cold extremes in eastern North America, North Asia (Figs. S149a-b), ~~and~~ South Asia (Figs. S159a-b), and Southern South America (Fig. 16a-b) during DJF, and primarily ~~warm events~~ warming events in Europe and western North America (Figs. S56c-d) during JJA. Comparing these processes associated with extreme DTDT changes with the mechanisms leading to usual temperature extremes (heat and cold waves) indicates similarities in the winter season when also temperature extremes are strongly affected by advection in many mid-latitude regions (Bieli et al., 2015; Nygård et al., 2023a; Röthlisberger and Papritz, 2023b; Kautz et al., 2022a), but larger differences in summer, when extreme DTDT events ~~and heatwave~~ are still primarily driven by advection (~~Harpaz et al., 2014; Sousa et al., 2019~~), but advection plays a smaller role, in particular especially for temperature extremes and heat waves in larger parts of the mid-latitudes ~~are not~~ (Zschenderlein et al., 2019; White et al., 2023, Röthlisberger and Papritz, 2023a).

We have studied the mechanisms associated with extreme DTDT changes in the tropics for two particular locations at 13°S in South America and South Africa (cf. Figs. S6S10-11 and S7) and found large differences between seasons. On the one hand, in JJA, advection is the main contributor to extreme DTDT changes, and interactions with the extratropics play a role, e.g., for the inflow of colder air masses towards lower latitudes during ~~cold events~~ cooling events upstream of a subtropical trough. This configuration resembles the circulation impacting the cold waves in Central South America (Marengo et al., 2023) and South Africa (Chikoore et al., 2024) in JJA 2021. On the other hand, during DJF, extreme DTDT changes occur primarily due to local-scale diabatic processes associated with changes from cloudy conditions with precipitation to less cloudy and drier conditions or vice versa. This points to an important role of cloud radiative effects, primarily through the reflection of solar radiation, for these events (cf. (Dai et al., 1999; Betts et al., 2013; Medvigy and Beaulieu, 2012).

Our study provides the first quantitative insights into the physical atmospheric processes that lead to extreme temperature changes from one day to another. The role of changing advection from warmer or colder regions for extreme DTDT changes is apparent across all studied regions except the tropics during DJF. Such advective effects are modified by Lagrangian temperature changes due to adiabatic or diabatic processes, which tend to either amplify or dampen extremely positive (warming events) and negative (~~cooling~~ events) DTDT changes, depending on the region and season. This dominant effect of advection also explains why the magnitude of DTDT changes is typically larger in the extratropics, where horizontal temperature gradients and wind velocities are larger compared to the tropics. Furthermore, the magnitude of the adiabatic and diabatic terms in our Lagrangian budgets is of the same magnitude in the extratropics and tropics and thus cannot compensate for this difference in advection. These mechanistic insights will be the basis for studying projected future changes in extreme DTDT changes in the second part of this study.

Appendix

The DTD (δ_T) change, as defined in Eq. (1), which has been determined based on the temperature 2m above the surface, is approximated through the average temperatures of the trajectories initiated on the corresponding day at their initiation time 0, denoted as δ_T^0 : ~~is an approximation, as the trajectories are initialized from different heights above the surface, assuming (and sampling) a well-mixed near-surface layer~~ is approximated through the average temperatures of the trajectories initiated on the corresponding day at their initiation time 0, denoted as δ_T^0 :

$$\delta_T \approx \delta_T^0 = \bar{T}_t^0 - \bar{T}_{t-1}^0$$

Note that the lower index here refers to the day on which the trajectories have been initiated, and the upper index refers to the time along the backward trajectory. This is an approximation, as the trajectories are initialized only once a day (while δ_T refers to daily average temperatures) and from different heights above the surface, assuming (and sampling) a well-mixed near-surface layer. These trajectory temperatures can then be expressed through the Lagrangian temperature evolution:

$$\begin{aligned} \delta_T^0 &= \bar{T}_t^0 - \bar{T}_{t-1}^0 \\ &= \bar{T}_t^0 - \bar{T}_t^{-3d} - \bar{T}_{t-1}^0 + \bar{T}_{t-1}^{-3d} + \bar{T}_t^{-3d} - \bar{T}_{t-1}^{-3d} \\ &= \Delta_{\bar{T},t} - \Delta_{\bar{T},t-1} + \delta_T^{-3d} \end{aligned} \quad (A1)$$

Here, ~~$\delta_T^{-3d} = \bar{T}_t^{-3d} - \bar{T}_{t-1}^{-3d}$ measures the contribution due to advection and $\Delta_{\bar{T},t} = \bar{T}_t^0 - \bar{T}_{t-1}^{-3d}$ and $\Delta_{\bar{T},t-1} = \bar{T}_{t-1}^0 - \bar{T}_{t-2}^{-3d}$ denotes the Lagrangian temperature change along the trajectories on a 3-day timescale for the previous day and the day of the event.~~ The term $\delta_T^{-3d} = \bar{T}_t^{-3d} - \bar{T}_{t-1}^{-3d}$ is used to measure the contribution due to advection.

~~We employed a different method to calculate the advection term than~~ This advection term differs from that of Röthlisberger and Papritz (2023b, a), who focused on daily temperature extremes and used horizontal advection of the air parcel along the climatological temperature gradient as a measure of advection in their temperature anomaly budget. This is not possible here, since our diagnostic is based on absolute temperatures and not on anomalies. ~~, whereas our approach differs in its formulation.~~ Technically, \bar{T}_t^{-3d} represents the average temperature of the air parcels initialized on the day of the extreme event, three days before they arrive at the target location, while \bar{T}_{t-1}^{-3d} represents the corresponding temperature for the air parcels initialized one day earlier. The expression in Eq. (A1), $\delta_T^{-3d} = \bar{T}_t^{-3d} - \bar{T}_{t-1}^{-3d}$ ~~thus, it~~ captures the difference in

temperature between the air parcels three days before their arrival. Assuming no further temperature changes occurred during transport, the DTD change would be solely due to these initial differences. This suggests that variations in the advection of air parcels with different original temperatures between the previous day and the day of the event cause temperature changes, which is referred to as an advection term [here](#).

The Lagrangian temperature change can be further decomposed into adiabatic and diabatic contributions using the thermodynamic energy Equation:

$$\frac{dT}{dt} = \frac{\kappa T \omega}{p} + \left(\frac{p}{p_0}\right)^\kappa \frac{d\theta}{dt} \quad (A2)$$

T is temperature. $\frac{dT}{dt}$ is the temperature change along the trajectory, $\kappa=0.286$, p denotes pressure ($p_0 = 1000$ hPa), ω vertical velocity in pressure coordinates, and θ the potential temperature.

Accordingly:

$$\Delta_{T,t} = \langle \int_{-3d}^0 \frac{dT_{t,i}}{d\tau} d\tau \rangle_i \quad (A3)$$

where $T_{t,i}$ is the temperature along the i^{th} trajectory, $\langle \dots \rangle_i = \sum_{i=1}^m \frac{1}{m} \dots$ denotes the average over the m trajectories and

τ is the time along the trajectory. Inserting (A3) into (A2) yields

$$\Delta_{T,t} = \Delta_{T,t}^{\text{adi}} + \Delta_{T,t}^{\text{dia}} \quad (A4)$$

$$\begin{aligned} \text{with the adiabatic term } (\Delta_{T,t}^{\text{adi}}) &= \langle \int_{-3d}^0 \frac{\kappa T \omega}{p} d\tau \rangle_i \\ &= \langle \int_{p^0}^{p^0} \frac{\kappa T}{p} dp \rangle_i \end{aligned}$$

$$\begin{aligned} \text{and the diabatic term } (\Delta_{T,t}^{\text{dia}}) &= \langle \int_{-3d}^0 \left(\frac{p}{p_0}\right)^\kappa \frac{d\theta}{d\tau} d\tau \rangle_i \\ &= \langle \int_{\theta^0}^{\theta^0} \left(\frac{p}{p_0}\right)^\kappa d\theta \rangle_i \end{aligned}$$

Then Eq. (A1) becomes

$$\begin{aligned} \delta_T^0 &= \delta_T^{-3d} + \Delta_{T,t}^{\text{adi}} - \Delta_{T,t-1}^{\text{adi}} + \Delta_{T,t}^{\text{dia}} - \Delta_{T,t-1}^{\text{dia}} \\ &= \delta_T^{-3d} + \delta_T^{\text{adi}} + \delta_T^{\text{dia}} \end{aligned} \quad (A5)$$

In Eq. (A5), δ_T^0 is the approximated near-surface DTD change, δ_T^{-3d} measures the mean temperature difference at the origin of the air parcels and thus the contribution of advection on a 3-day time scale, δ_T^{adi} is the mean temperature difference created through adiabatic compression or expansion resulting from vertical descent or ascent, respectively, and δ_T^{dia} is the contribution of mean diabatic heating or cooling from processes such as latent heating in clouds, radiation, and surface fluxes.

Code and data availability

The code of the trajectory model LAGRANTO is available at <https://iacweb.ethz.ch/staff/sprenger/lagranto/download.html> (Sprenger and Wernli, 2015). The HadGHCND and BEST –datasets used in this study can be freely accessed from <http://www.metoffice.gov.uk/hadobs/hadghcnd/download.html> and <http://berkeleyearth.org/data/>. ERA5 data are available via the Copernicus Climate Change Service (C3S; <https://doi.org/10.24381/cds.143582cf>; Hersbach et al., 2018).

Author contributions

Both authors designed the study. KH performed the analysis, produced the figures, and drafted the manuscript. Both authors discussed the results and edited the manuscript.

Competing interests

Stephan Pfahl is the executive editor of WCD.

Acknowledgments

We acknowledge the HPC service of ZEDAT, Freie Universität Berlin, for providing computational Resources (Bennett et al., 2020).

References

- Adams, R. E., Lee, C. C., Smith, E. T., and Sheridan, S. C.: The relationship between atmospheric circulation patterns and extreme temperature events in North America, *International Journal of Climatology*, 41, 92-103, 2021.
- Bennett, L., Melchers, B., and Proppe, B.: Curta: a general-purpose high-performance computer at ZEDAT, Freie Universität Berlin, 2020.
- Betts, A. K., Desjardins, R., and Worth, D.: Cloud radiative forcing of the diurnal cycle climate of the Canadian Prairies, *Journal of Geophysical Research: Atmospheres*, 118, 8935-8953, 2013.
- Bieli, M., Pfahl, S., and Wernli, H.: A Lagrangian investigation of hot and cold temperature extremes in Europe, *Quarterly Journal of the Royal Meteorological Society*, 141, 98-108, 2015.
- Böker, B., Laux, P., Olschewski, P., and Kunstmann, H.: Added value of an atmospheric circulation pattern-based statistical downscaling approach for daily precipitation distributions in complex terrain, *International Journal of Climatology*, 2023.

- 805 Byrne, M. P.: Amplified warming of extreme temperatures over tropical land, *Nature Geoscience*, 14, 837-841, 2021.
- Chan, E. Y. Y., Goggins, W. B., Kim, J. J., and Griffiths, S. M.: A study of intracity variation of temperature-related mortality and socioeconomic status among the Chinese population in Hong Kong, *J Epidemiol Community Health*, 66, 322-327, 2012.
- 810 Chikoore, H., Mbokodo, I. L., Singo, M. V., Mohomi, T., Munyai, R. B., Havenga, H., Mahlobo, D. D., Engelbrecht, F. A., Bopape, M.-J. M., and Ndarana, T.: Dynamics of an extreme low temperature event over South Africa amid a warming climate, *Weather and Climate Extremes*, 44, 100668, 2024.
- Dai, A. and Deng, J.: Arctic amplification weakens the variability of daily temperatures over northern middle-high latitudes, *Journal of Climate*, 34, 2591-2609, 2021.
- 815 Dai, A., Trenberth, K. E., and Karl, T. R.: Effects of clouds, soil moisture, precipitation, and water vapor on diurnal temperature range, *Journal of Climate*, 12, 2451-2473, 1999.
- Dirmeyer, P. A., Sridhar Mantripragada, R. S., Gay, B. A., and Klein, D. K.: Evolution of land surface feedbacks on extreme heat: Adapting existing coupling metrics to a changing climate, *Frontiers in Environmental Science*, 1650, 2022.
- Ghil, M. and Lucarini, V.: The physics of climate variability and climate change, *Reviews of Modern Physics*, 92, 035002, 2020.
- 820 Gough, W.: Theoretical considerations of day-to-day temperature variability applied to Toronto and Calgary, Canada data, *Theoretical and Applied Climatology*, 94, 97-105, 2008.
- ~~Harpaz, T., Ziv, B., Saaroni, H., and Beja, E.: Extreme summer temperatures in the East Mediterranean dynamical analysis, *International Journal of Climatology*, 34, 2014.~~
- 825 Hartig, K., Tziperman, E., and Loughner, C. P.: Processes contributing to North American cold air outbreaks based on air parcel trajectory analysis, *Journal of Climate*, 36, 931-943, 2023.
- Hersbach, H.: Global reanalysis: goodbye ERA-Interim, hello ERA5, *ECMWF newsletter*, 159, 17, 2019.
- 830 Hersbach, H., Bell, B., Berrisford, P., Hirahara, S., Horányi, A., Muñoz-Sabater, J., Nicolas, J., Peubey, C., Radu, R., Schepers, D., Simmons, A., Soci, C., Abdalla, S., Abellan, X., Balsamo, G., Bechtold, P., Biavati, G., Bidlot, J., Bonavita, M., Chiara, G. D., Dahlgren, P., Dee, D., Diamantakis, M., Dragani, R., Flemming, J., Forbes, R., Fuentes, M., Geer, A., Haimberger, L., Healy, S., Hogan, R. J., Hólm, E., Janisková, M., Keeley, S., Laloyaux, P., Lopez, P., Lupu, C., Radnoti, G., Rosnay, P. d., Rozum, I., Vamborg, F., Villaume, S., and Thépaut, J.-N.: The ERA5 global reanalysis, *Quarterly Journal of the Royal Meteorological Society*, 146, 1999-2049, 10.1002/qj.3803, 2020.
- Horton, D. E., Johnson, N. C., Singh, D., Swain, D. L., Rajaratnam, B., and Diffenbaugh, N. S.: Contribution of changes in atmospheric circulation patterns to extreme temperature trends, *Nature*, 522, 465-469, 2015.

- 835 Hovdahl, I.: The deadly effect of day-to-day temperature variation in the United States, *Environmental Research Letters*, 17, 104031, 2022.
- Karl, T. R., Knight, R. W., and Plummer, N.: Trends in high-frequency climate variability in the twentieth century, *Nature*, 377, 217-220, 1995.
- 840 ~~Kautz, L. A., Martius, O., Pfahl, S., Pinto, J. G., Ramos, A. M., Sousa, P. M., and Woollings, T.: Atmospheric blocking and weather extremes over the Euro-Atlantic sector – a review, *Weather and climate dynamics*, 3, 305–336, 2022a.~~
- Kautz, L. A., Martius, O., Pfahl, S., Pinto, J. G., Ramos, A. M., Sousa, P. M., and Woollings, T.: Atmospheric blocking and weather extremes over the Euro-Atlantic sector – a review, *Weather Clim. Dynam.*, 3, 305-336, 10.5194/wcd-3-305-2022, 2022b.
- 845 Kotz, M., Wenz, L., Stechemesser, A., Kalkuhl, M., and Levermann, A.: Day-to-day temperature variability reduces economic growth, *Nature Climate Change*, 11, 319-325, 2021.
- Krauskopf, T. and Huth, R.: Trends in intraseasonal temperature variability in Europe: Comparison of station data with gridded data and reanalyses, *International Journal of Climatology*, 44, 3054-3074, 2024.
- Lee, D. Y., Lin, W., and Petersen, M. R.: Wintertime Arctic Oscillation and North Atlantic Oscillation and their impacts on the Northern Hemisphere climate in E3SM, *Climate Dynamics*, 55, 1105-1124, 2020.
- 850 Linsenmeier, M.: Temperature variability and long-run economic development, *Journal of Environmental Economics and Management*, 121, 102840, 2023.
- Liu, G., Li, J., and Ying, T.: Atlantic multi-decadal oscillation modulates the relationship between El Niño-Southern Oscillation and fire weather in Australia, *Atmospheric Chemistry and Physics Discussions*, 2023, 1-17, 2023.
- 855 Magaritz-Ronen, L. and Raveh-Rubin, S.: Tracing the formation of exceptional fronts driving historical fires in Southeast Australia, *npj Climate and Atmospheric Science*, 6, 110, 2023.
- Marengo, J., Espinoza, J., Bettolli, L., Cunha, A., Molina-Carpio, J., Skansi, M., Correa, K., Ramos, A., Salinas, R., and Sierra, J.-P.: A cold wave of winter 2021 in central South America: characteristics and impacts, *Climate Dynamics*, 1-23, 2023.
- 860 Matuszko, D., Twardosz, R., and Piotrowicz, K.: Relationships between cloudiness, precipitation and air temperature, *Geographia Polonica*, 77, 9-18, 2004.
- Medvigy, D. and Beaulieu, C.: Trends in daily solar radiation and precipitation coefficients of variation since 1984, *Journal of Climate*, 25, 1330-1339, 2012.
- ~~Nygård, T., Papritz, L., Naakka, T., and Vihma, T.: Cold wintertime air masses over Europe: Where do they come from and how do they form?, *EGUsphere*, 2023, 1–31, 2023a.~~

- 865 Nygård, T., Papritz, L., Naakka, T., and Vihma, T.: Cold wintertime air masses over Europe: where do they come from and how do they form?, *Weather and Climate Dynamics*, 4, 943-961, 2023^b.
- Parker, T. J., Berry, G. J., and Reeder, M. J.: The influence of tropical cyclones on heat waves in Southeastern Australia, *Geophysical Research Letters*, 40, 6264-6270, 2013.
- Pfahl, S.: Characterising the relationship between weather extremes in Europe and synoptic circulation features, *Natural Hazards and Earth System Sciences*, 14, 1461-1475, 2014.
- 870 Pfahl, S. and Wernli, H.: Quantifying the relevance of atmospheric blocking for co-located temperature extremes in the Northern Hemisphere on (sub-) daily time scales, *Geophysical Research Letters*, 39, 2012.
- Piskala, V. and Huth, R.: Asymmetry of day-to-day temperature changes and its causes, *Theoretical and Applied Climatology*, 140, 683-690, 2020.
- 875 Quinting, J. F. and Reeder, M. J.: Southeastern Australian heat waves from a trajectory viewpoint, *Monthly Weather Review*, 145, 4109-4125, 2017.
- Rohde, R. A. and Hausfather, Z.: The Berkeley Earth land/ocean temperature record, *Earth System Science Data Discussions*, 2020, 1-16, 2020.
- Röthlisberger, M. and Papritz, L.: Quantifying the physical processes leading to atmospheric hot extremes at a global scale, 880 *Nature Geoscience*, 16, 210-216, 2023a.
- Röthlisberger, M. and Papritz, L.: A Global Quantification of the Physical Processes Leading to Near-Surface Cold Extremes, *Geophysical Research Letters*, 50, e2022GL101670, 2023b.
- Santos, J. A., Pfahl, S., Pinto, J. G., and Wernli, H.: Mechanisms underlying temperature extremes in Iberia: a Lagrangian perspective, *Tellus A: Dynamic Meteorology and Oceanography*, 67, 26032, 2015.
- 885 Sarmiento, J. H.: Into the tropics: Temperature, mortality, and access to health care in Colombia, *Journal of Environmental Economics and Management*, 119, 102796, 2023.
- Schumacher, D. L., Keune, J., Van Heerwaarden, C. C., Vilà-Guerau de Arellano, J., Teuling, A. J., and Miralles, D. G.: Amplification of mega-heatwaves through heat torrents fuelled by upwind drought, *Nature Geoscience*, 12, 712-717, 2019.
- 890 Sharma, S., Chen, Y., Zhou, X., Yang, K., Li, X., Niu, X., Hu, X., and Khadka, N.: Evaluation of GPM-Era satellite precipitation products on the southern slopes of the Central Himalayas against rain gauge data, *Remote Sensing*, 12, 1836, 2020.
- Sheridan, S. C., Lee, C. C., and Smith, E. T.: A comparison between station observations and reanalysis data in the identification of extreme temperature events, *Geophysical Research Letters*, 47, e2020GL088120, 2020.

- 895 Sillmann, J., Croci-Maspoli, M., Kallache, M., and Katz, R. W.: Extreme cold winter temperatures in Europe under the influence of North Atlantic atmospheric blocking, *Journal of Climate*, 24, 5899-5913, 2011.
- Simmons, A. J.: Trends in the tropospheric general circulation from 1979 to 2022, *Weather and Climate Dynamics*, 3, 777-809, 2022.
- 900 ~~Sousa, P. M., Barriopedro, D., Ramos, A. M., García Herrera, R., Espírito Santo, F., and Trigo, R. M.: Saharan air intrusions as a relevant mechanism for Iberian heatwaves: The record breaking events of August 2018 and June 2019, *Weather and Climate Extremes*, 26, 100224, 2019.~~
- Sun, J. and Mahrt, L.: Relationship of surface heat flux to microscale temperature variations: Application to BOREAS, *Boundary-Layer Meteorology*, 76, 291-301, 1995.
- Wan, H., Kirchmeier-Young, M., and Zhang, X.: Human influence on daily temperature variability over land, *Environmental Research Letters*, 16, 094026, 2021.
- 905 Wang, F., Vavrus, S. J., Francis, J. A., and Martin, J. E.: The role of horizontal thermal advection in regulating wintertime mean and extreme temperatures over interior North America during the past and future, *Climate Dynamics*, 53, 6125-6144, 2019.
- White, R. H., Anderson, S., Booth, J. F., Braich, G., Draeger, C., Fei, C., Harley, C. D., Henderson, S. B., Jakob, M., and Lau, C.-A.: The unprecedented Pacific Northwest heatwave of June 2021, *Nature Communications*, 14, 727, 2023.
- 910 Wu, Y., Li, S., Zhao, Q., Wen, B., Gasparrini, A., Tong, S., Overcenco, A., Urban, A., Schneider, A., and Entezari, A.: Global, regional, and national burden of mortality associated with short-term temperature variability from 2000–19: a three-stage modelling study, *The Lancet Planetary Health*, 6, e410-e421, 2022a.
- Wu, Y., Wen, B., Li, S., Gasparrini, A., Tong, S., Overcenco, A., Urban, A., Schneider, A., Entezari, A., and Vicedo-Cabrera, A. M.: Fluctuating temperature modifies heat-mortality association around the globe, *The Innovation*, 3, 2022b.
- 915 Xu, Z., Huang, F., Liu, Q., and Fu, C.: Global pattern of historical and future changes in rapid temperature variability, *Environmental Research Letters*, 15, 124073, 2020.
- Zhou, X., Wang, Q., and Yang, T.: Decreases in days with sudden day-to-day temperature change in the warming world, *Global and Planetary Change*, 192, 103239, 2020.
- 920 Zschenderlein, P., Fink, A. H., Pfahl, S., and Wernli, H.: Processes determining heat waves across different European climates, *Quarterly Journal of the Royal Meteorological Society*, 145, 2973-2989, 2019.